

Strain gradient stabilization with dual stress points for the meshfree nodal integration method in inelastic analyses

Cheng-Tang Wu^{1,*}, Sheng-Wei Chi², Masataka Koishi³ and Youcai Wu⁴

¹Livermore Software Technology Corporation (LSTC), 7374 Las Positas Road Livermore, 94550, CA, USA

²University of Illinois at Chicago, Chicago, 60607-7023, IL, USA

³Koishi Laboratory, Yokohama Rubber Co. Ltd., Tokyo, Japan

⁴Karagozian & Case, 700 N Brand Blvd, Suite 700 Glendale, 91203, CA, USA

SUMMARY

A nonlinear nodal-integrated meshfree Galerkin formulation based on recently proposed strain gradient stabilization (SGS) method is developed for large deformation analysis of elastoplastic solids. The SGS is derived from a decomposed smoothed displacement field and is introduced to the standard variational formulation through the penalty method for the inelastic analysis. The associated strain gradient matrix is assembled by a B-bar method for the volumetric locking control in elastoplastic materials. Each meshfree node contains two coinciding integration points for the integration of weak form by the direct nodal integration scheme. As a result, a nonlinear stabilized nodal integration method with dual nodal stress points is formulated, which is free from stabilization control parameters and integration cells for meshfree computation. In the context of extreme large deformation analysis, an adaptive anisotropic Lagrangian kernel approach is introduced to the nonlinear SGS formulation. The resultant Lagrangian formulation is constantly updated over a period of time on the new reference configuration to maintain the well-defined displacement gradients as well as strain gradients in the Lagrangian computation. Several numerical benchmarks are studied to demonstrate the effectiveness and accuracy of the proposed method in large deformation inelastic analyses. Copyright © 2015 John Wiley & Sons, Ltd.

Received 13 April 2015; Revised 23 September 2015; Accepted 21 October 2015

KEY WORDS: meshfree method; nonlinear; nodal integration; stabilization

1. INTRODUCTION

Thanks for the characteristics of discretization flexibility and customized approximation, meshfree or particle methods have undergone extensive developments and led to widespread applications in interdisciplinary sciences and engineering over the past two decades. In particular, significant research efforts have been spent on the nodally integrated meshfree or particle methods because of the conceptual simplicity and the reduced numerical restriction in modeling large deformation, moving discontinuity, and immersed problems in solid and structural applications [1–6]. Nevertheless, the application of a direct nodal integration (DNI) scheme to the weak form of meshfree or particle methods suffers from the presence of spurious or zero-energy modes [7] in many solid mechanics problems. The presence of these undesired deformation modes in Galerkin-based meshfree methods is mainly caused by the rank instability in the integration of weak form by the central difference formula from the DNI scheme. A number of linear and nonlinear stabilization methods have been developed to suppress the unstable deformation modes caused by the DNI scheme.

*Correspondence to: Cheng-Tang Wu, Livermore Software Technology Corporation (LSTC), 7374 Las Positas Road, Livermore, CA 94551, USA.

†E-mail: ctwu@lstc.com

The Galerkin/least-squares stabilization approach developed by Beissel and Belytschko [7] is one of the earliest stabilization methods for meshfree nodal integration method. This method belongs to a type of residual stabilization in which a least-squares form of the residual is added into the Lagrangian functional in a consistent manner. Although this method enables the solution of partial differential equations without a need of background cells for integration, the optimal choice of the stabilization control parameter remains an open question. The second type of stabilization methods is the approach based on the physical stabilization technique [8]. In general, the physical stabilization is obtained by the Taylor series expansion of the displacement gradient matrix up to certain higher-order terms. These higher-order terms are introduced to nodal integration formulation for the enhancement of the coercivity and provide the stabilization that is free of control parameters. Nevertheless, a common feature of those physical stabilization methods [9, 10] is the requirement of background cells for the numerical integration. Like the Galerkin/least-squares stabilization method, most meshfree physical stabilization methods were developed for the linear analysis. On the other hand, Chen *et al.* [1, 11] developed a stabilized conforming nodal integration (SCNI) method in which a strain-smoothing scheme was introduced as a stabilization process for nodal integration. To further stabilize the SCNI solution in nonlinear analysis, a modified SCNI method, which combines the ‘stress points’ [12] technique and penalty approach, was introduced (Figure 2). Essentially, the SCNI technique based on conforming approximations and compatible background cells in strain smoothing suffers from the numerical difficulty when the deformation is beyond the applicability of Lagrangian material description. For that reason, a stabilized nonconforming nodal integration (SNNI) method was developed and adopted in extremely large deformation simulations [13–15]. The SNNI method releases the restrictive compatibility requirements in the SCNI method by introducing a semi-Lagrangian kernel [13] into the nonconforming integration cells [3]. This modification makes the SNNI method independent of the choice of integration cells whose purpose is to provide enough accuracy and stabilization in severe deformation analyses. Recent study has shown [16] that additional accuracy and stabilization in the SNNI method can be achieved by the reduction of solution errors of PDEs from quadrature inaccuracy using the higher-order exactness integration [17]. An alternative SCNI formulation was also developed by Wang and Li [18] for the stabilization and regularization of damage-induced strain localization solution [19]. This nodal integration formulation was derived from the nonlocal meshfree methodology [20] using a two-level strain-smoothing procedure for the stabilization calculation. However, this method cannot preclude the use of background cells for integration.

The meshfree nodal integration method based on background cells poses some significant challenges from both the mathematical formulation and the programming aspects in the simulation of severe deformation problems. Most notably, the strain operator in this family must be invertible stable and well defined in the large deformation analysis. From the best of authors’ knowledge, only limited literatures have been published on the scope of purely nodal integration for the meshfree Galerkin method in large deformation analysis. Wu *et al.* [21] developed the smoothed particle Galerkin (SPG) method in which a smoothed displacement field is introduced to stabilize the meshfree Galerkin nodal integration solution in large deformation and damage analyses. Recently, the displacement smoothing technique in SPG method has been adopted in the SCNI method for the simulation of concrete impact problems [22]. It was shown [23] that SPG method is closely related to the nonlocal meshfree method [20] by means of strain regularization analysis. In order to recover the locality of strain approximation for non-failure analysis, Wu *et al.* [23] has introduced a strain gradient stabilization (SGS) scheme to the meshfree Galerkin nodal integration method. In their approach, the strain gradients are derived based on the decomposed strain field from the displacement smoothing in the SPG method. It leads to a penalty formulation with the penalty (stabilization) parameter coming naturally from the enhanced strain field. The resultant stabilization formulation in [23] does not require the background cells for the domain integration. Their linear analysis results indicate that the norm of penalty error in the SGS method is close to an optimal convergence rate of $O(h)$, where h denotes the size of nodal spacing in discretization.

The goal of this paper is to obviate the inherent limitation of cell-based meshfree nodal integration method in the large deformation inelastic analysis. This is achieved by exploring the use of the stabilization scheme in linear SGS method [23] with the well-known B-bar method [24] for the

derivation of nonlinear nodal integration formulation in elastoplastic applications. The rest of paper is organized as follows: In the next section, we provide an overview on the SGS method in the linear elasticity analysis. In Section 3, we present a nonlinear version of SGS method for large deformation inelastic analysis. Both quasi-static and explicit dynamic formulations are derived. The corresponding discrete equations are given in the same section. Section 4 presents a nonlinear SGS formulation based on an adaptive Lagrangian kernel approximation for the extremely large deformation analysis. Several numerical examples are presented in Section 5 to illustrate the robustness and accuracy of the method. Final remarks are drawn in Section 6.

2. OVERVIEW ON THE STRAIN GRADIENT STABILIZATION FORMULATION IN LINEAR ELASTICITY

Following the work in [23], the SGS method for linear elastic analysis is formulated by the penalty approach through the introduction of a penalty term associated with an enhanced strain field to the standard functional:

$$\bar{\Pi}(\mathbf{u}) = \arg \min_{\mathbf{u} \in H^1(\Omega^0)} \left[\Pi(\mathbf{u}) + \frac{1}{2} \int_{\Omega^0} \left(\bar{\Theta}(\boldsymbol{\varepsilon}(\mathbf{u})) - \boldsymbol{\varepsilon}(\mathbf{u}) \right)^T : \mathbf{C} : \left(\bar{\Theta}(\boldsymbol{\varepsilon}(\mathbf{u})) - \boldsymbol{\varepsilon}(\mathbf{u}) \right) d\Omega \right] \quad (1)$$

subject to

$$\mathbf{u} = \mathbf{u}_g \quad \text{on } \Gamma_g \quad (2)$$

where \mathbf{u} is the displacement field, \mathbf{C} is the elasticity tensor, $\Omega^0 \subset \mathbb{R}^2$ is a bounded polygon with the smoothed boundary $\partial\Omega^0$, \mathbf{u}_g is the imposed displacement on the essential boundary Γ_g , $\Pi(\mathbf{u})$ stands for the standard functional in linear elasticity, and the term $\left(\bar{\Theta}(\boldsymbol{\varepsilon}(\mathbf{u})) - \boldsymbol{\varepsilon}(\mathbf{u}) \right)$ represents the enhanced strain field that provides the stabilization effect in the nodal integration method. $\bar{\Theta}(\boldsymbol{\varepsilon}(\mathbf{u}))$ denotes the stabilized strain that is defined by [23]

$$\bar{\Theta}(\boldsymbol{\varepsilon}(\mathbf{u})) \equiv \nabla \mathbf{u} + \bar{\nabla}^{(2)} \mathbf{u} = \boldsymbol{\varepsilon}(\mathbf{u}) + \bar{\nabla}^{(2)} \mathbf{u} \quad (3)$$

The stabilized strain in Equation (3) consists of the regular strain field $\boldsymbol{\varepsilon}(\mathbf{u}) = \nabla \mathbf{u}$ and the enhanced strain field $\bar{\nabla}^{(2)} \mathbf{u}$. The notation $\bar{\nabla}^{(2)}$ is a second-order gradient operator defined by [23]

$$\bar{\nabla}^{(2)} \mathbf{u} \equiv \frac{1}{2} \left(\nabla \boldsymbol{\eta} : \mathbf{u} \nabla^{(2)} + (\nabla \boldsymbol{\eta} : \mathbf{u} \nabla^{(2)})^T \right) \quad (4)$$

or in index form

$$\left[\bar{\nabla}^{(2)} \mathbf{u} \right]_{ij} = \frac{1}{2} \left(\eta_{kl,i} u_{m,nj} \delta_{lm} \delta_{kn} + u_{k,li} \eta_{mn,j} \delta_{km} \delta_{ln} \right) \quad (5)$$

where $\nabla^{(2)}$ denotes the standard second-order gradient operator and $\boldsymbol{\eta}(X)$ is a tensor form of position-dependent coefficients defined by [23]

$$\boldsymbol{\eta}(X) \equiv \frac{1}{2!} \int_{\Omega^0} \tilde{\Psi}(Y; X) (Y - X)^{(2)} d\Omega \quad (6)$$

where $\tilde{\Psi}$ is called the displacement smoothing function [23]. We first remark that $|\boldsymbol{\eta}(X_I)| \propto h^2$, which is proportional to a length squared. This implies that the usage of strain gradient operator $\bar{\Theta}$ of Equation (3) in functional (1) will lead to a point-wise truncation error of $O(h^2)$ in the penalty term. This term is going to vanish as the discretization size h goes to 0. Secondly, no explicit penalty/stabilization parameter is involved in functional (1). Indeed, the penalty form in functional (1) can be viewed as a type of least-squares stabilization, where the h^2 penalty parameter is imbedded in the formulation and the residual of the penalty term is provided to stabilize the solution. In linear elasticity, the enhanced stress field is written as

$$\tilde{\boldsymbol{\sigma}} = \mathbf{C} : \left(\bar{\nabla}^{(2)} \mathbf{u} \right) \quad (7)$$

With the introduced enhanced strain field, the minimization problem of (1) leads to the following stabilized discrete weak form by the nodal integration method, which only requires a space \mathbf{U}^h for $\hat{\mathbf{u}}$:

$$a^h(\hat{\mathbf{u}}, \delta \hat{\mathbf{u}}) = l(\delta \hat{\mathbf{u}}) \quad \forall \delta \hat{\mathbf{u}} \in \mathbf{U}_0^h \quad (8)$$

where

$$\begin{aligned} a^h(\hat{\mathbf{u}}, \delta \hat{\mathbf{u}}) &= \int_{\Omega^0} \delta(\nabla \hat{\mathbf{u}})^T : \mathbf{C} : (\nabla \hat{\mathbf{u}}) d\Omega + \int_{\Omega^0} \delta(\bar{\nabla}^{(2)} \hat{\mathbf{u}})^T : \mathbf{C} : (\bar{\nabla}^{(2)} \hat{\mathbf{u}}) d\Omega \\ &= a_{stan}^h(\hat{\mathbf{u}}, \delta \hat{\mathbf{u}}) + a_{stab}^h(\hat{\mathbf{u}}, \delta \hat{\mathbf{u}}) \end{aligned} \quad (9)$$

$$l(\delta \hat{\mathbf{u}}) = \int_{\Omega^0} \delta \hat{\mathbf{u}} \cdot \mathbf{f} d\Omega + \int_{\Gamma_N} \delta \hat{\mathbf{u}} \cdot \mathbf{t} d\Gamma \quad (10)$$

Here, \mathbf{f} is the body force; \mathbf{t} is the traction applied on the Neumann boundary Γ_N . The space \mathbf{U}_0^h consists of functions in the Sobolev space $\mathbf{H}^1(\Omega^0)$ that vanishes on the boundary in the sense of traces. The notation a_{stan}^h in Equation (9) denotes the standard bilinear form. The stabilized bilinear form a_{stab}^h is defined by

$$\begin{aligned} a_{stab}^h(\hat{\mathbf{u}}, \delta \hat{\mathbf{u}}) &= \int_{\Omega^0} \delta(\bar{\Theta}^h(\epsilon(\hat{\mathbf{u}})) - \epsilon(\hat{\mathbf{u}}))^T : \mathbf{C} : (\bar{\Theta}^h(\epsilon(\hat{\mathbf{u}})) - \epsilon(\hat{\mathbf{u}})) d\Omega \\ &= \int_{\Omega^0} \delta(\bar{\nabla}^{(2)} \hat{\mathbf{u}})^T : \mathbf{C} : (\bar{\nabla}^{(2)} \hat{\mathbf{u}}) d\Omega \end{aligned} \quad (11)$$

where $\bar{\Theta}^h$ is the discrete analogue of $\bar{\Theta}$. The previous stabilization term is added into the standard bilinear term to enhance the coercivity of the formulation in the nodal integration method. The final discrete equations for the linear elasticity analysis are summarized in the following:

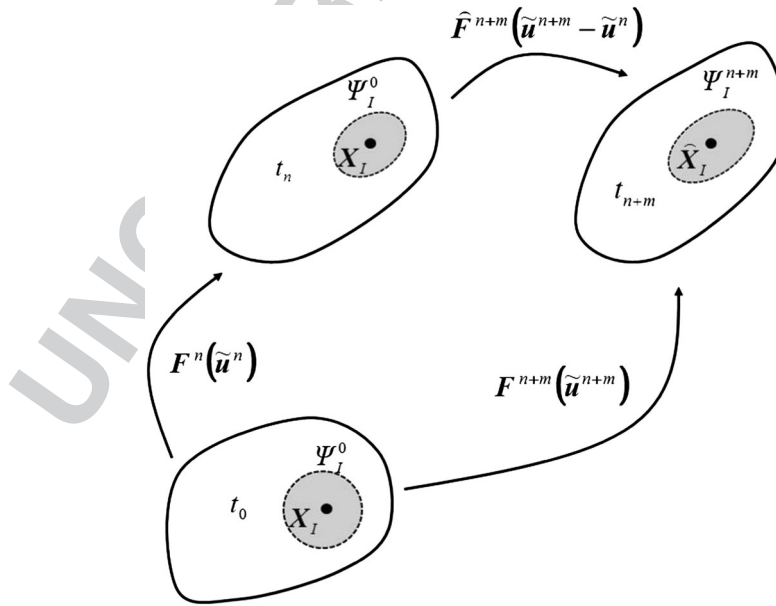


Figure 1. Illustration of a neighbor particle reconstruction step for the computation of deformation gradient in nonlinear SGS method.

$$(K + \tilde{K}) \tilde{U} = f^{ext} \quad (12)$$

$$K_{IJ} = \sum_{K=1}^{NP} B_I^T(X_K) C B_J(X_K) V_K^0 \quad (13)$$

$$\tilde{K}_{IJ} = \sum_{K=1}^{NP} \tilde{B}_I^T(X_K) C \tilde{B}_J(X_K) V_K^0 \quad (14)$$

$$f_I^{ext} = \sum_{K=1}^{NP} \Psi_I(X_K) f(X_K) V_K^0 + \sum_{K=1}^{NB} \Psi_I(X_K) t(X_K) L_K \quad (15)$$

$$B_I(X) = \begin{bmatrix} \frac{\partial \Psi_I(X)}{\partial X} & 0 \\ \frac{\partial \Psi_I(X)}{\partial Y} & \frac{\partial \Psi_I(X)}{\partial Y} \\ 0 & \frac{\partial \Psi_I(X)}{\partial Y} \end{bmatrix} \quad (16)$$

$$\tilde{B}_I(X) = \begin{bmatrix} \tilde{b}_{I11} & \tilde{b}_{I12} \\ \tilde{b}_{I21} & \tilde{b}_{I22} \\ \tilde{b}_{I31} & \tilde{b}_{I32} \end{bmatrix} \quad (17)$$

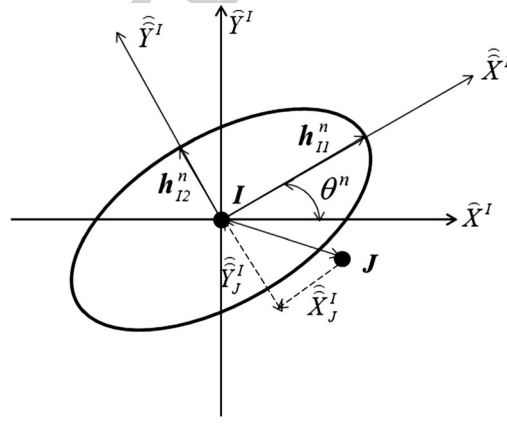


Figure 2. Ellipsoidal nodal support in adaptive anisotropic Lagrangian kernel approach.

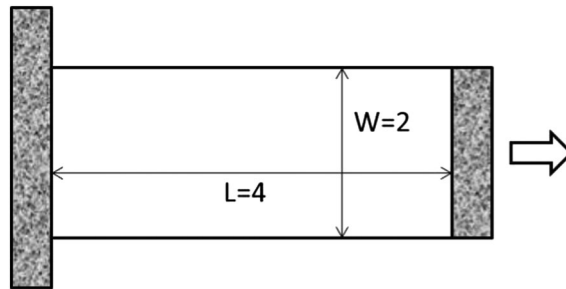


Figure 3. A simple tension test model.

where vector $\tilde{\mathbf{U}} = [\tilde{\mathbf{u}}_1 \ \tilde{\mathbf{u}}_2 \ \cdots \ \tilde{\mathbf{u}}_{NP}]$ contains the problem unknowns for generalized nodal displacements [25, 26]. NP denotes the total number of meshfree nodes in discretization. V_I^0 stands for the volume of node I . NB denotes the number of boundary nodes, and L_k is the length associated with the boundary node along the global boundary. The meshfree shape function Ψ in Equation (16) and the displacement smoothing function $\tilde{\Psi}$ in Equation (6) are considered to be the same as those in [23]. They are constructed using the first-order meshfree convex approximation by generalized meshfree approximation method (see [25] for detailed mathematical derivation and [27–29] for formulations in solid mechanics applications). Meshfree convex approximation possesses the Kronecker-delta property [30] at the boundary and therefore avoids special numerical treatments to enforce the essential boundary condition in general solid mechanics applications. The coefficients in the strain gradient matrix of Equation (17) can be found in [23] and thus are omitted in this paper.

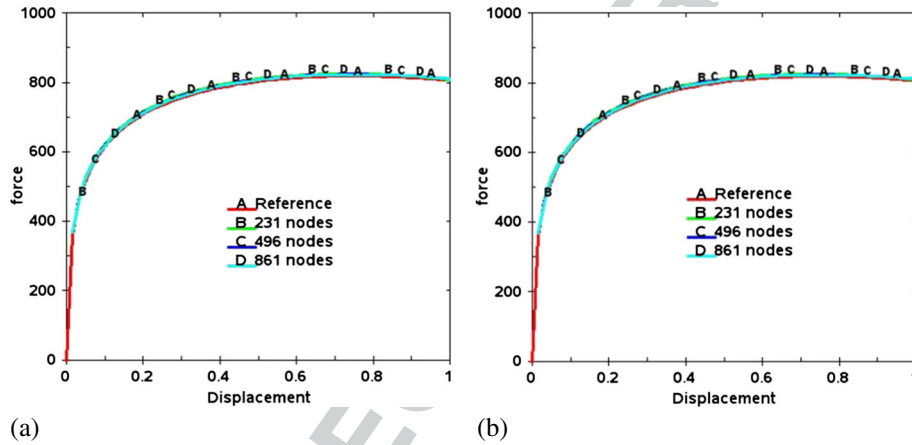


Figure 4. Reaction force response with different uniform discretization in quasi-static analysis. (a) direct nodal integration method and (b) present method.

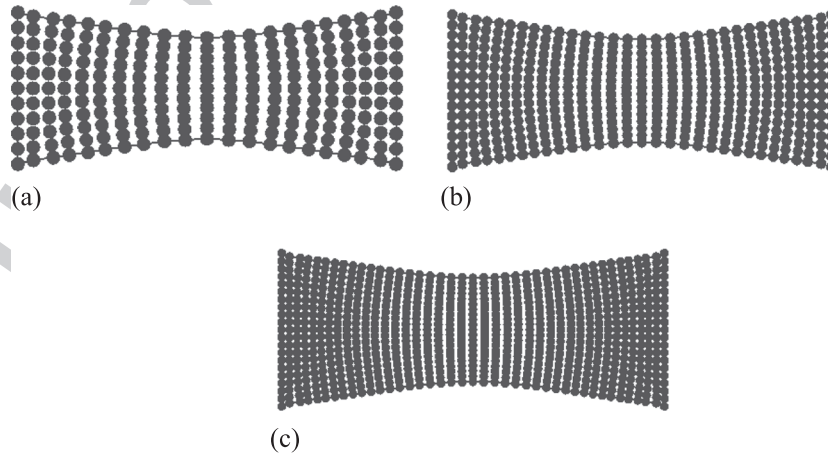


Figure 5. The deformation of direct nodal method with different uniform discretization at $d = 1.0$ in quasi-static analysis. (a) 231 nodes; (b) 496 nodes; and (c) 861 nodes.

3. STRAIN GRADIENT STABILIZATION FORMULATION FOR INELASTIC ANALYSIS

The stabilized discrete weak form for linear elasticity in Equation (8) is extended to cover the non-linear cases through an updated Lagrangian formulation with reference to the current configuration in the inelastic analysis:

$$\delta \bar{\Pi} = \int_{\Omega} \delta (\nabla \hat{\mathbf{u}})^T : \boldsymbol{\sigma} d\Omega + \int_{\Omega} \delta \left(\bar{\nabla}^{(2)} \hat{\mathbf{u}} \right)^T : \tilde{\boldsymbol{\sigma}} d\Omega - l^{ext} \quad (18)$$

where $\boldsymbol{\sigma}$ is the regular Cauchy stress and $\tilde{\boldsymbol{\sigma}}$ is the enhanced stress field. Note that both stress quantities are defined at the current configuration Ω . l^{ext} corresponds to the nonlinear version of external work in Equation (8). Similar to most finite element stabilization methods in nonlinear solid and structural analysis [31], the enhanced stress field in inelasticity is obtained by replacing the elastic tensor \mathbf{C} in Equation (7) with a material response tensor (elastoplastic tangent modulus) \mathbf{C}^{σ} as

$$\tilde{\boldsymbol{\sigma}} = \mathbf{C}^{\sigma} : \left(\bar{\nabla}^{(2)} \hat{\mathbf{u}} \right) \quad (19)$$

The linearization of Equation (18) with a neglect of nonlinear contribution in the enhanced strain field yields

$$\Delta \delta \bar{\Pi} = \int_{\Omega} \delta (\nabla \hat{\mathbf{u}})^T : (\mathbf{C}^{\sigma} + \mathbf{T}^{\sigma}) : \Delta (\nabla \hat{\mathbf{u}}) d\Omega + \int_{\Omega} \delta \left(\bar{\nabla}^{(2)} \hat{\mathbf{u}} \right)^T : \mathbf{C}^{\sigma} : \Delta \left(\bar{\nabla}^{(2)} \hat{\mathbf{u}} \right) d\Omega - \Delta l^{ext} \quad (20)$$

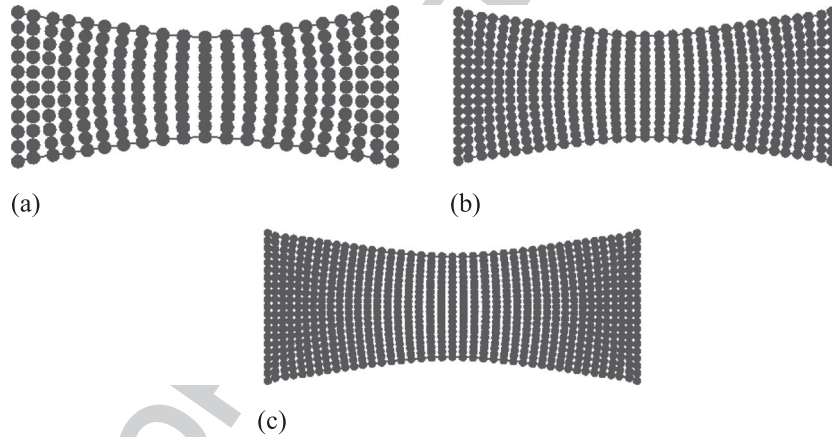


Figure 6. The deformation of present method with different uniform discretization at $d = 1.0$ in quasi-static analysis. (a) 231 nodes; (b) 496 nodes; and (c) 861 nodes.

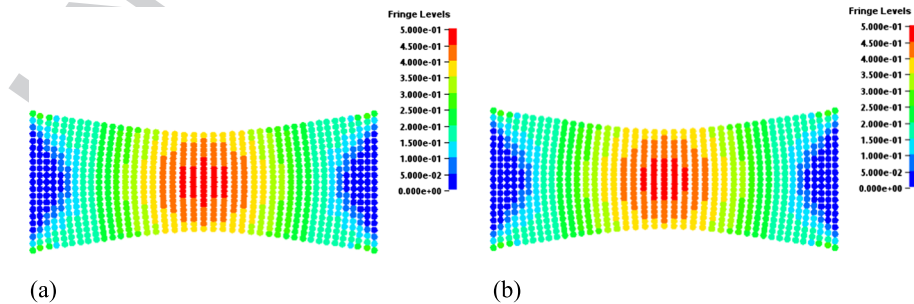


Figure 7. Comparison of effective plastic strain with 861 nodes model. (a) direct nodal integration method and (b) present method.

where T^σ is the regular geometric response tensor that is given by

$$T_{ijkl}^\sigma = \delta_{ik} \sigma_{jl} \quad (21)$$

Considering that the Lagrangian meshfree shape function $\Psi_I^0 = \Psi_I(X)$ [26, 32] and the gradients of displacement and strain approximations that are defined in the undeformed configuration, the variational equation of Equation (20) is transformed from the current configuration Ω to the undeformed configuration Ω^0 as

$$\begin{aligned} \Delta \delta \bar{\Pi} = & \int_{\Omega^0} \delta \left(F^{-1} \nabla^0 \hat{u} \right)^T : (C^\sigma + T^\sigma) : \Delta \left(F^{-1} \nabla^0 \hat{u} \right) J^0 d\Omega \\ & + \int_{\Omega^0} \delta \left(F^{-1} \bar{\nabla}^{(2)0} \hat{u} \right)^T : C^\sigma : \Delta \left(F^{-1} \bar{\nabla}^{(2)0} \hat{u} \right) J^0 d\Omega - \Delta l^{ext} \end{aligned} \quad (22)$$

where

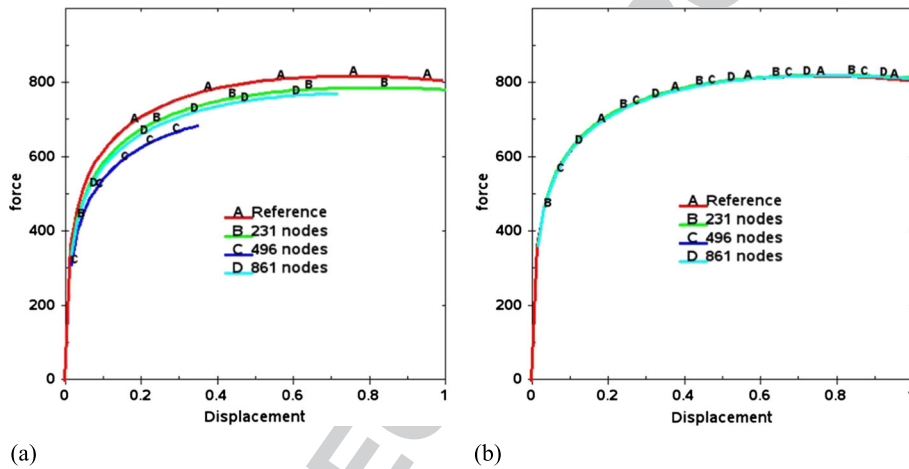


Figure 8. Reaction force response with different nonuniform discretization in quasi-static analysis. (a) direct nodal integration method and (b) present method.

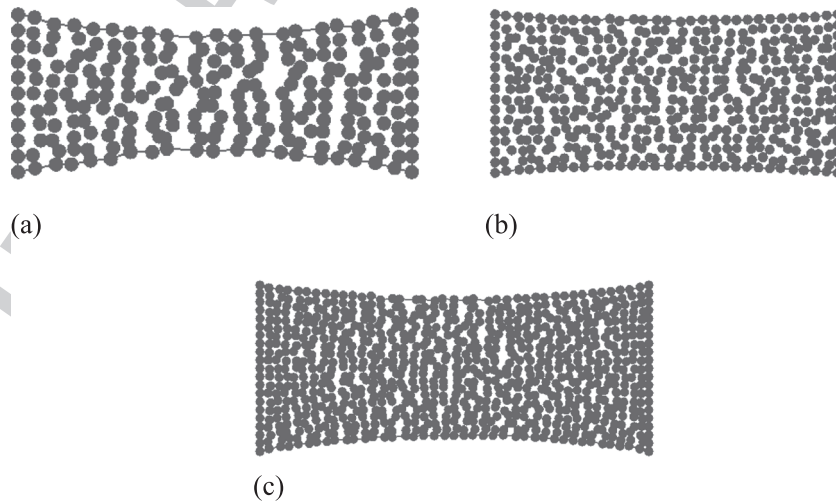


Figure 9. The deformation of direct nodal integration method with different nonuniform discretization in quasi-static analysis. (a) 231 nodes (at $d = 1.0$); (b) 496 nodes (at $d = 0.33$); and (c) 861 nodes (at $d = 0.68$).

$$[\nabla^0 \hat{\mathbf{u}}]_{ij} = \frac{\partial \hat{u}_i}{\partial X_j} \quad (23)$$

$$\left[\bar{\nabla}^{(2)0} \hat{\mathbf{u}} \right]_{ij} = \frac{1}{2} \left(\sum_{k=1}^2 \sum_{l=1}^2 \frac{\partial \eta_{kl}}{\partial X_i} \frac{\partial^2 \hat{u}_l}{\partial X_k \partial X_j} + \sum_{k=1}^2 \sum_{l=1}^2 \frac{\partial^2 \hat{u}_l}{\partial X_i \partial X_k} \frac{\partial \eta_{lk}}{\partial X_j} \right) \quad (24)$$

$$\hat{u}_i = \sum_{l=1}^{NP} \Psi_l^0 \tilde{u}_l, i = 1, 2 \quad (25)$$

$F_{ij} = \frac{\partial x_i}{\partial X_j}$ is the deformation gradient, which is obtained using the DNI scheme. J^0 is the determinant of the deformation gradient. The introduction of meshfree convex approximation in Equation (25) into Equation (22) results in the following incremental discrete equation for the evaluation of nodal displacements:

$$\left(\mathbf{K}^M + \mathbf{K}^G + \tilde{\mathbf{K}}^{dev} \right)_{n+1}^v (\Delta \tilde{\mathbf{U}})_{n+1}^{v+1} = \mathbf{R}_{n+1}^v \quad (26)$$

where all the functions are computed in the v th iteration during the $(n+1)$ th time incremental step. \mathbf{K}^M and \mathbf{K}^G are corresponding regular stiffness matrices for material and geometrical nonlinearity,

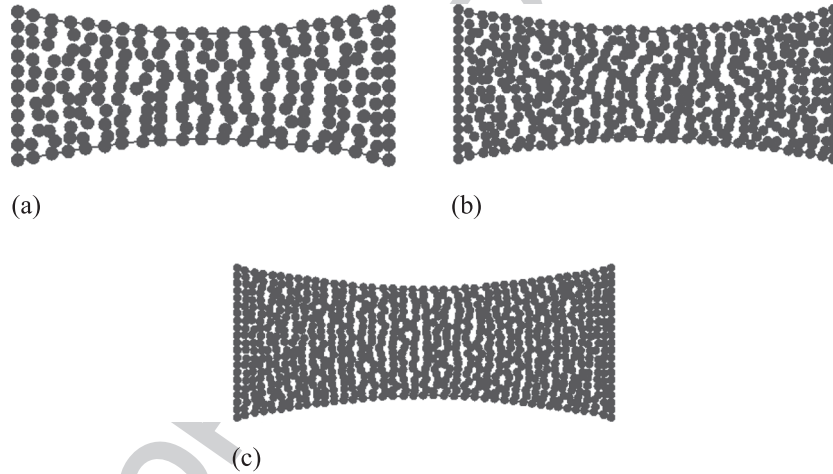


Figure 10. The deformation of present method with different nonuniform discretization at $d = 1.0$ in quasi-static analysis. (a) 231 nodes; (b) 496 nodes; and (c) 861 nodes.

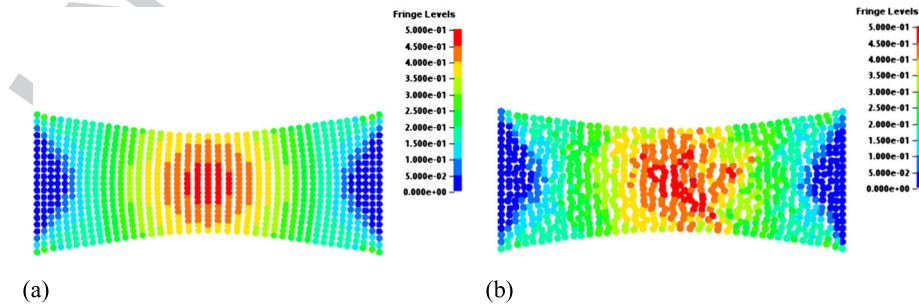


Figure 11. Comparison of effective plastic strain of present method with 861 nodes model at $d = 1.0$ in quasi-static analysis. (a) uniform discretization and (b) nonuniform discretization.

respectively. The explicit expression of those two stiffness matrices can be found elsewhere in text-books and literatures [26, 33]; therefore, it is omitted here. Because plasticity for either small or large deformation is based on nearly incompressible material behavior, only the deviatoric part of the strain gradient matrix is considered for the stabilization calculation in inelastic problems. This is similar to the B-bar approach [24] for the volumetric locking control in nearly incompressible materials. The modified stabilized stiffness counterpart $\tilde{\mathbf{K}}_{IJ}^{dev}$ using the B-bar method and DNI scheme can be expressed by

$$\tilde{\mathbf{K}}_{IJ}^{dev} = \int_{\Omega^0} \tilde{\mathbf{B}}_I^{devT} \mathbf{C}^\sigma \tilde{\mathbf{B}}_J^{dev} J^0 d\Omega \stackrel{DNI}{=} \sum_{K=1}^{NP} \tilde{\mathbf{B}}_I^{devT}(\mathbf{X}_K) \mathbf{C}^\sigma \tilde{\mathbf{B}}_J^{dev}(\mathbf{X}_K) J^0(\mathbf{X}_K) V_K^0 \quad (27)$$

where the modified strain gradient matrix $\tilde{\mathbf{B}}_I^{dev}$ is given by

$$\tilde{\mathbf{B}}_I^{dev}(\mathbf{X}) = \begin{bmatrix} \tilde{b}_{I11} & \tilde{b}_{I12} \\ \tilde{b}_{I21} & \tilde{b}_{I22} \\ \tilde{b}_{I31} & \tilde{b}_{I32} \end{bmatrix} \quad (28)$$

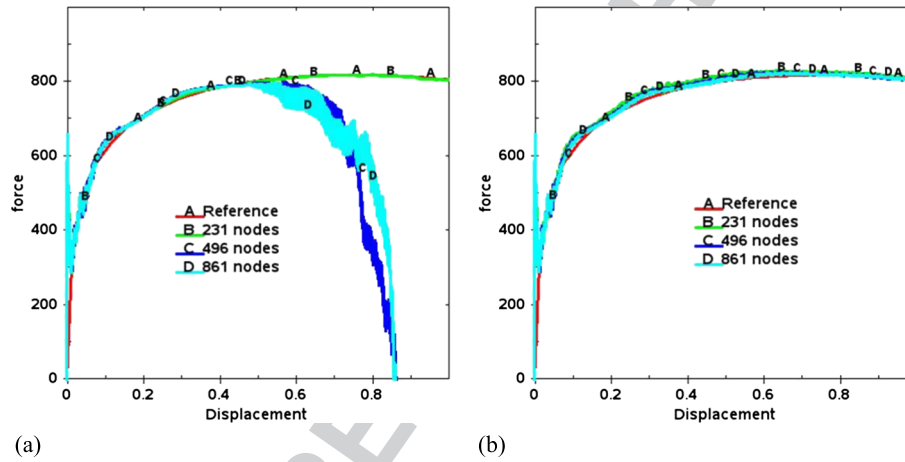


Figure 12. Reaction force response with different uniform discretization in explicit dynamic analysis. (a) direct nodal integration method and (b) present method.

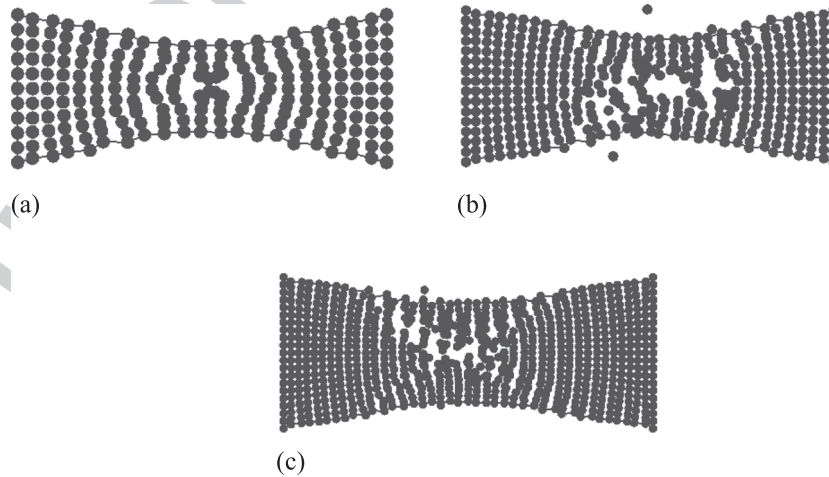


Figure 13. The deformation of direct nodal integration method with different uniform discretization at $d = 1.0$ in explicit dynamic analysis. (a) 231 nodes; (b) 496 nodes; and (c) 861 nodes.

with its components

$$\tilde{\tilde{b}}_{I11} = F_{11}^{-1}(\tilde{b}_{I11} - \tilde{b}_{Iv1}) + F_{12}^{-1}(\tilde{b}_{I12} - \tilde{b}_{Iv2}) \quad (29)$$

$$\tilde{\tilde{b}}_{I12} = F_{21}^{-1}(\tilde{b}_{I11} - \tilde{b}_{Iv1}) + F_{22}^{-1}(\tilde{b}_{I12} - \tilde{b}_{Iv2}) \quad (30)$$

$$\tilde{\tilde{b}}_{I21} = F_{11}^{-1}\tilde{b}_{I21} + F_{12}^{-1}\tilde{b}_{I22} \quad (31)$$

$$\tilde{\tilde{b}}_{I22} = F_{21}^{-1}\tilde{b}_{I21} + F_{22}^{-1}\tilde{b}_{I22} \quad (32)$$

$$\tilde{\tilde{b}}_{I31} = F_{11}^{-1}(\tilde{b}_{I31} - \tilde{b}_{Iv1}) + F_{12}^{-1}(\tilde{b}_{I32} - \tilde{b}_{Iv2}) \quad (33)$$

$$\tilde{\tilde{b}}_{I32} = F_{21}^{-1}(\tilde{b}_{I31} - \tilde{b}_{Iv1}) + F_{22}^{-1}(\tilde{b}_{I32} - \tilde{b}_{Iv2}) \quad (34)$$

$$\tilde{b}_{Iv1} = \frac{(\tilde{b}_{I11} + \tilde{b}_{I31})}{3} \quad (35)$$

$$\tilde{b}_{Iv2} = \frac{(\tilde{b}_{I12} + \tilde{b}_{I32})}{3} \quad (36)$$

Finally, the residual term along with the stabilized internal force term are expressed in a conventional way by

$$\mathbf{R} = \mathbf{f}^{ext} - \mathbf{f}^{int} - \tilde{\mathbf{f}}^{stab} \quad (37)$$

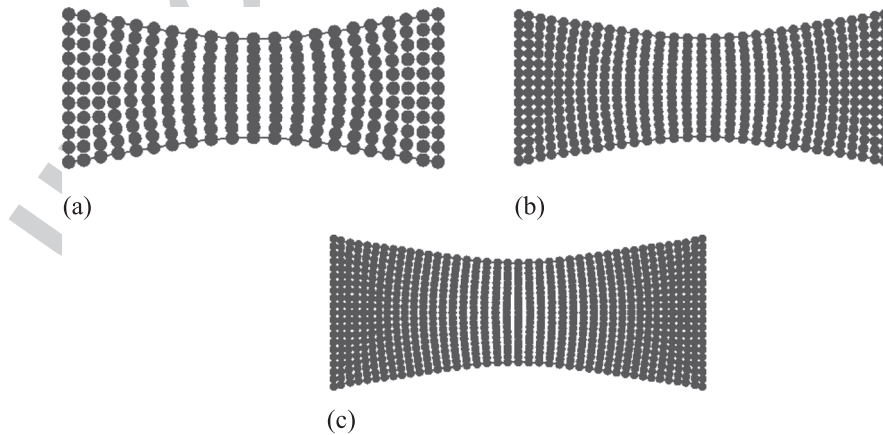


Figure 14. The deformation of present method with different uniform discretization at $d = 1.0$ in explicit dynamic analysis. (a) 231 nodes; (b) 496 nodes; and (c) 861 nodes.

where \mathbf{f}^{ext} and \mathbf{f}^{int} are regular external force vector and internal force vector [26, 33], respectively. The stabilized force vector is computed by DNI scheme as

$$\tilde{\mathbf{f}}_I^{stab} = \int_{\Omega^0} \tilde{\mathbf{B}}_I^{devT} \tilde{\boldsymbol{\sigma}} J^0 d\Omega \stackrel{DNI}{=} \sum_{K=1}^{NP} \tilde{\mathbf{B}}_I^{devT} (X_K) \tilde{\boldsymbol{\sigma}}(X_K) J^0 V_K^0 \quad (38)$$

where $\tilde{\boldsymbol{\sigma}}^T = (\tilde{\sigma}_{11}, \tilde{\sigma}_{12}, \tilde{\sigma}_{22})$ is a vector containing the component of Cauchy stress associated with the stabilization and is updated by

$$\tilde{\boldsymbol{\sigma}}_{n+1} = \tilde{\boldsymbol{\sigma}}_n + \Delta \tilde{\boldsymbol{\sigma}}_{n+1} = \tilde{\boldsymbol{\sigma}}_n + (\mathbf{C}^\sigma)_{n+1} \left(\tilde{\mathbf{B}}^{dev} \right)_{n+1} \Delta \tilde{\mathbf{U}}_{n+1} \quad (39)$$

In other words, each meshfree node in the present stabilized meshfree nodal integration method carries two stress points, one for regular nodal stress $\boldsymbol{\sigma}$ and the other for the enhanced nodal stress $\tilde{\boldsymbol{\sigma}}$. This dual stress point integration scheme is different from existing meshfree nodal integration

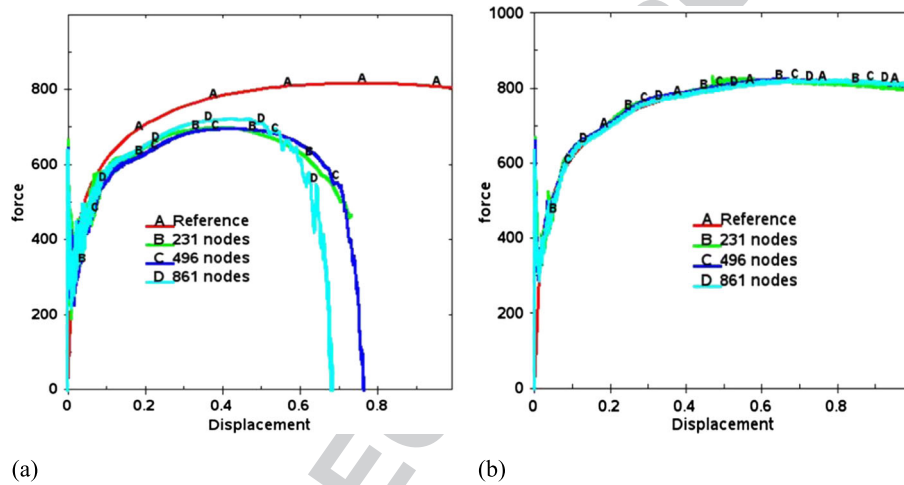


Figure 15. Reaction force response with different nonuniform discretization in explicit dynamic analysis. (a) direct nodal integration method and (b) present method.

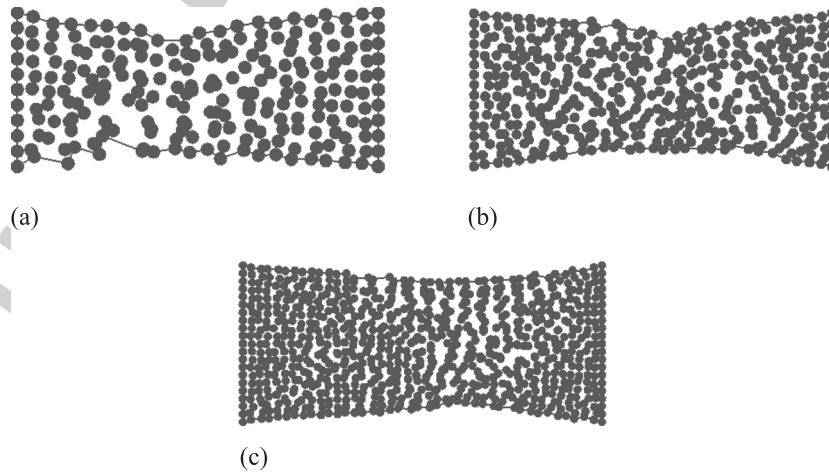


Figure 16. The deformation of direct nodal integration method with different nonuniform discretization in explicit dynamic analysis. (a) 231 nodes (at $d = 0.7$); (b) 496 nodes (at $d = 0.7$); and (c) 861 nodes (at $d = 0.6$).

schemes based on the physical stabilization technique [9, 10] where background cells and multiple stress points are usually needed for the stabilization calculation.

Subsequently, the discrete equations for explicit dynamic analysis can also be obtained by

$$\mathbf{M}\mathbf{a} = \mathbf{f}^{ext} - \mathbf{f}^{int} - \tilde{\mathbf{f}}^{stab} \quad (40)$$

$$\mathbf{M}_I = \sum_{K=1}^{NP} \rho^0 \Psi_I(\mathbf{X}_K) V_K^0 \mathbf{I}_{[2 \times 2]} \quad (41)$$

where \mathbf{M}_I is the lumped nodal mass matrix and ρ^0 is the initial material density. In the explicit dynamics analysis, the numerical evaluation of stabilized force vector using Equation (39) is computationally unfeasible because it involves the determination of elastoplastic tangent modulus at each explicit time step. As suggested by Belytschko and Lee [34], the elastoplastic tangent modulus in Equation (39) can be replaced by a modified shear modulus \tilde{G} for the stabilized stress update, that is,

$$2\tilde{G} = \sqrt{\frac{H_{\Delta\tau}}{H_{\Delta e}}} \quad (42)$$

where

$$H_{\Delta\tau} = \frac{1}{2} \sum_{i=1}^2 \sum_{j=1}^2 \Delta\tau_{ij} \Delta\tau_{ij}, H_{\Delta e} = \frac{1}{2} \sum_{i=1}^2 \sum_{j=1}^2 \Delta e_{ij} \Delta e_{ij} \quad (43)$$

$\Delta\tau_{ij}$ and Δe_{ij} are components of the deviatoric part of the stress and strain increments, respectively, which are obtained from the regular nodal stress and strain computation using the DNI scheme. As a consequence, the incremental stabilized stress vector is computed in the explicit dynamic analysis by

$$\Delta\tilde{\sigma} \approx 2\tilde{G} \left(\tilde{\mathbf{B}}^{dev} \right) \Delta\tilde{\mathbf{U}} \quad (44)$$

The critical time step Δt_c for the central difference time integration in the explicit dynamic analysis is governed by the Courant–Friedrichs–Lewy condition. The eigenvalue inequality theorem [33, 35] has been applied to the meshfree Galerkin method with first-order convex approximation [36] for the

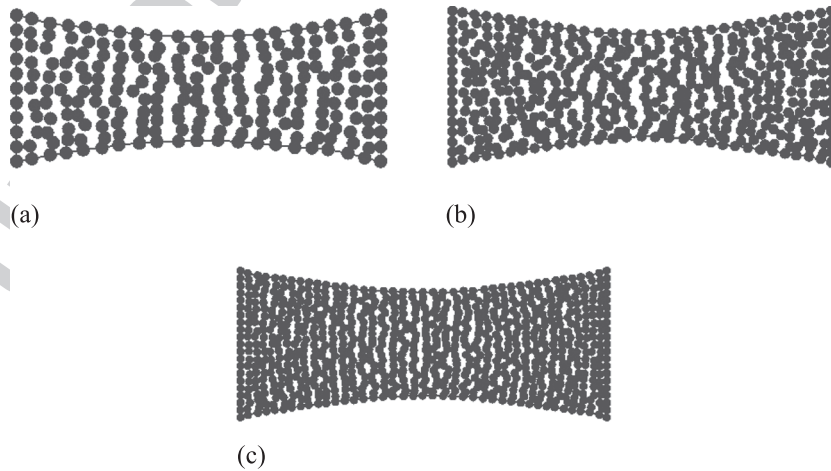


Figure 17. The deformation of present method with different nonuniform discretization at $d = 1.0$ in explicit dynamic analysis. (a) 231 nodes; (b) 496 nodes; and (c) 861 nodes.

critical time step analysis. With the additional stabilization term, the critical time step is modified to be

$$\Delta t_c = \frac{2}{\sqrt{\max_{I=1, NP} (\lambda_{\max}^I)}} \quad (45)$$

$$\lambda_{\max}^I \leq c^2 \max \left(\sum_{J=1}^{NP} \frac{\Psi_{J,x}^2(\mathbf{X}_I) + \Lambda_J(\mathbf{X}_I)}{\Psi_J(\mathbf{X}_I)}, \sum_{J=1}^{NP} \frac{\Psi_{J,y}^2(\mathbf{X}_I) + \Lambda_J(\mathbf{X}_I)}{\Psi_J(\mathbf{X}_I)} \right) \quad (46)$$

$$\Lambda_J(\mathbf{X}_I) = \tilde{b}_{J11}^2(\mathbf{X}_I) + \tilde{b}_{J21}^2(\mathbf{X}_I) + \tilde{b}_{J31}^2(\mathbf{X}_I) + \tilde{b}_{J12}^2(\mathbf{X}_I) + \tilde{b}_{J22}^2(\mathbf{X}_I) + \tilde{b}_{J32}^2(\mathbf{X}_I) \quad (47)$$

where c is the material sound speed. The spatial derivatives of the Lagrangian shape function in inequality (46) are computed using the chain rule given by

$$\Psi_{J,i}(\mathbf{X}) = \Psi_{J,i}^0 = \frac{\partial \Psi_J^0}{\partial x_i} = \frac{\partial \Psi_J^0}{\partial X_j} \frac{\partial X_j}{\partial x_i}, i = 1, 2 \quad (48)$$

The explicit dynamic analysis using Equation (45) gives a conservative estimation of critical time step but the very stable results in the nodal integration method. A sharp estimation of critical time step is not the goal in this paper but will be considered in the future. On the other hand, it is known that the critical time step in the explicit dynamic analysis may drop significantly in the large deformation simulation using the pure Lagrangian method because of the near singularity of the inverse of deformation gradient in Equation (48). In meshfree methods, this numerical obstacle can be sidestepped by an incorporation of adaptive Lagrangian kernel [13–15, 37] that is updated constantly over a period of time in the simulation as described in the following section.

4. ADAPTIVE ANISOTROPIC LAGRANGIAN KERNEL FOR SEVERE DEFORMATION ANALYSIS

Similar to most Lagrangian finite element and meshfree methods, the pure Lagrangian formulation of present stabilized nodal integration method is unable to handle the severe deformation that is beyond the applicability of Lagrangian material description. In other words, the determinant of the deformation gradient could become $J^0 = \det(\mathbf{F}) < 0$, which leads to a negative volume in the computation and fails to advance the numerical simulation. One effective way to solve this numerical problem is to reconstruct the regular displacement gradient matrix \mathbf{B} and the stabilized strain gradient matrix $\tilde{\mathbf{B}}^{dev}$ constantly over a period of time on the new reference configuration. Similar technique of reconstructing the neighbor particle information has already been adapted in other particle/meshfree methods [13–15, 37] for the large deformation analysis. The main difference between the present approach and existing techniques [13–15, 37] is an update of Lagrangian kernel based on the deformation gradient from SGS formulation. We refer this numerical procedure as an adaptive anisotropic Lagrangian kernel approach in this study.

Using the chain rule, the calculation for the deformation gradient can be written as

$$\mathbf{F}^{n+m} = \hat{\mathbf{F}}^{n+m} \mathbf{F}^n \quad (49)$$

where $\hat{\mathbf{F}}^{n+m}(\bar{\mathbf{x}})$ is the decomposed deformation gradient, from $t = t_n$ to t_{n+m} , computed based on the new reference configuration and is given by

$$\hat{\mathbf{F}}_{ij}^{n+m}(\mathbf{X}_J) = \frac{\partial \hat{x}_i}{\partial \hat{X}_j} = \sum_{l=1}^{NP} \frac{\partial \Psi_l}{\partial \hat{X}_j}(\hat{\mathbf{X}}_J) \hat{x}_{il} \quad (50)$$

Here, $\hat{x} = \hat{X} + \tilde{u}(X, t_{n+m})$ is a position vector defined in the new reference configuration $\hat{X} = x(X, t_n)$. Figure 1 illustrates a neighbor particle reconstruction step for the computation of deformation/gradient at time $t = t_{n+m}$ in the present nonlinear SGS method. Because this particle-based reconstruction step for the computation of deformation gradient does not involve remeshing as that in the r/h-adaptive finite element methods, the remapping procedures that interpolate the internal variables at the integration points from the old mesh to the new mesh are not necessary.

Considering the anisotropic deformation in large deformation inelastic analysis, an ellipsoidal nodal support is used for the neighbor particle searching in each new reference configuration $\hat{X} = x(X, t_n)$. In two dimensions, a local \hat{X}^I -coordinate system in which the axes are parallel to the global Cartesian coordinates and with its origin located at \hat{X}_I is defined for each meshfree node I . The

ellipsoid of each meshfree node I is defined by another local $\hat{X}^I\hat{X}$ -coordinate system formed by a dyad of mutually perpendicular vectors $h_{II}^n, i = 1, 2$, the semimajor axes of the ellipsoid as shown in Figure 2.

The two-dimensional ellipsoidal cubic spline kernel function can be defined in the local \hat{X}^I -coordinate system by

$$\phi(\hat{X}_J - \hat{X}_I) = \phi_1\left(\frac{\hat{X}_J^I}{h_1^n}\right) \phi_1\left(\frac{\hat{Y}_J^I}{h_2^n}\right) \quad (51)$$

where $h_1^n = |h_{11}^n|$ and $h_2^n = |h_{22}^n|$ are the semimajor axes of the ellipsoid. \hat{X}_J^I and \hat{Y}_J^I are the projections of relative position vector $\hat{X}_J - \hat{X}_I$ on the local \hat{X}^I -coordinate system, respectively. ϕ_1 is the standard one-dimensional cubic spline kernel function [26]. In general, we have $h_1^0 = h_2^0$ as a circular shape cubic spline kernel function at $t = 0$. The circular shape domain of cubic spline kernel function deforms and rotates according to the Lagrangian motion between each two adaptive Lagrangian kernel steps. In this study, the evolution of ellipsoid is determined by the right Cauchy–Green deformation tensor

$$\mathbf{G}^n = (\mathbf{F}^n)^T \cdot \mathbf{F}^n = \sum_{i=1}^2 (\lambda_i^n)^2 \mathbf{n}_i \otimes \mathbf{n}_i \quad (52)$$

where $\lambda_i^n, i = 1, 2$ are two distinct principal stretches and $\mathbf{n}_i = [n_{xi}, n_{yi}]^T, i = 1, 2$ are the corresponding eigenvectors. Therefore, the length and direction of the semi-axes of ellipsoid are estimated by the eigenvalues and eigenvectors, respectively, of the matrix \mathbf{G}^n . In other words, the eigenvalues of \mathbf{G}^n represent two principal stretches of the ellipsoid at $t = t_n$. As a consequence, the semimajor axes of the ellipsoid are approximated by

$$h_1^n = \lambda_1^n h_1^0 \quad \text{and} \quad h_2^n = \lambda_2^n h_2^0 \quad (53)$$

and the vectors $h_{ii}^n = h_i^n \mathbf{n}_i = h_i^n [n_{xi} \ n_{yi}]^T, i = 1, 2$ are obtained. The gradients of the two-dimensional ellipsoidal cubic spline kernel function needed in the computation of displacement gradient matrix \mathbf{B} and the stabilized strain gradient matrix $\tilde{\mathbf{B}}^{dev}$ can also be evaluated by

$$\begin{aligned} \nabla_{\hat{X}} \left(\phi(\hat{X}_J - \hat{X}_I) \right)_i &= \left(\frac{h_{ii}^n}{h_i^n} \right) \cdot \nabla_{\hat{X}} \left(\phi(\hat{X}_J - \hat{X}_I) \right) \\ &= n_{xi} \frac{\partial \phi_1\left(\frac{\hat{X}_J^I}{h_1^n}\right)}{\partial \hat{X}} + n_{yi} \frac{\partial \phi_1\left(\frac{\hat{Y}_J^I}{h_2^n}\right)}{\partial \hat{Y}}, i = 1, 2 \end{aligned} \quad (54)$$

5. NUMERICAL EXAMPLES

In this section, five benchmark examples are analyzed to study the performance of present stabilization method in inelastic problems. Plain strain condition is assumed in two-dimensional problems. Unless otherwise specified, a normalized nodal support size of 1.5 is used in the meshfree computation. A dimensionless unit system is adopted in most examples for convenience. A standard Newton–Raphson method is employed to solve the nonlinear equation (26). If the number of iterations reaches the maximum number of 10, the execution of quasi-static analysis is terminated.

5.1. Tension test

In this example, the large deformation in a simple tension test is analyzed. The aluminum test specimen with one end fixed and the other end subjected to a prescribed displacement is considered as shown in Figure 3. The material has an initial density $\rho^0 = 2700$. The strain-hardening elastic-plastic material properties are as follows: Young's modulus $E = 69,000.0$, Poisson's ratio $\nu = 0.3$, and an isotropic hardening rule $\sigma_y(\bar{\epsilon}^p) = \sigma_y^0 (1 + \alpha \bar{\epsilon}^p)^\beta$ with coefficients $\beta = 0.216$, $\sigma_y^0 = 80.5992$, and $\alpha = 10,000.0$. $\sigma_y(\bar{\epsilon}^p)$ is the flow stress that is a scalar and increases monotonically with the effective plastic strain. Three levels of model refinements are used, with 21×11 , 31×16 , and 41×21 equally spaced nodes. Alternatively, three corresponding nonuniform refinement models are also generated for the test. Because the analytical solution of this problem is not available, a volumetric locking-free solution obtained from the meshfree-enriched finite element method [27, 28] using the 41×21 uniform discretization model by quasi-static analysis is adopted as a reference for comparison.

5.1.1. Quasi-static analysis. The problem is first analyzed by the quasi-static analysis carried out using 60 equal loading steps. The convergence of reaction force response is reported in Figure 4(a) and (b) for the DNI method and the present method, respectively. Both nodal integration solutions are comparable and agree very well with the reference solution. The final deformation plots for the DNI method and the present method are given in Figures 5 and 6, respectively. Surprisingly, all three deformation plots generated by the direct integration method do not display any spurious or zero-energy modes. The results in Figures 4–6 indicate that the direct integration method is able to produce a stable quasi-static solution under uniform discretization in the tension mode. The comparison of effective plastic strain in two 861 nodes models is shown Figure 7 that shows a good agreement with each other. Overall, the difference between the DNI method and the present method is marginal in this test case.

The convergence study of reaction force response in nonuniform discretization is given in Figure 8(a) and (b) for the direction nodal integration method and the present method, respectively. The results in Figure 8(a) show that the direction nodal integration method is not monotonically converged. Indeed, the final solution of DNI method never converges in the 496 nodes and 861 nodes models. The divergence of the solution in nonuniform discretization can be attributed to the under-integration nature of the direction nodal integration method. This phenomenon is consistent with

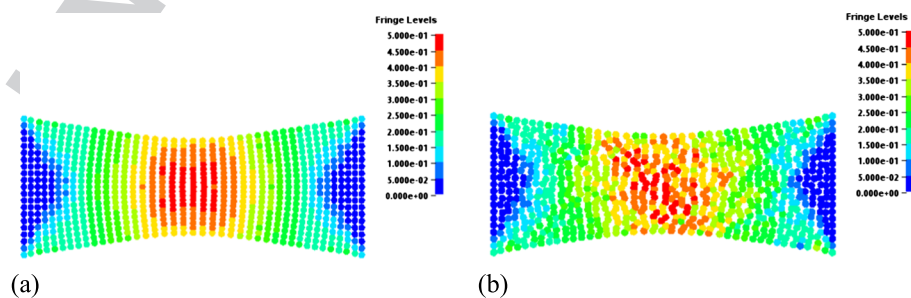


Figure 18. Comparison of effective plastic strain of present method with 861 nodes model at $d = 1.0$ in explicit dynamic analysis. (a) uniform discretization and (b) nonuniform discretization.

the softer force response observed in Figure 8(a) and is confirmed by the visible unstable modes displayed in deformation plot shown in Figure 9. On the other hand, the reaction force solution of the present method is more accurate than that of the direction nodal integration method as shown in Figure 8(b). All implicit runs in three discretization models converge until the final stage with the deformed plots provided in Figure 10. The comparable effective plastic strain contours in the present solution using 861 nodes model are given in Figure 11(a) and (b) for the uniform and nonuniform discretization, respectively. The comparison results in Figures 8–11 suggest that the present method is able to stabilize the direction nodal integration solution in this simple tension test using the nonuniform discretization.

5.1.2. Explicit dynamics analysis. Superior performance of the present stabilization method over the DNI method is also presented in the accuracy comparison by the explicit dynamic analysis. A very low speed of displacement control is imposed on the test model to mimic the quasi-static state in the explicit dynamic analysis. In the case of uniform discretization, the direction nodal integration method behaves as well as that in the quasi-static analysis from the small to moderated deformation stage as shown in Figure 12(a). However, the direction nodal integration method suffers from the zero-energy modes in the large deformation range as shown in Figure 13. As a result, the method produces the solution that is much softer than the reference solution. The poor performance in the DNI method can be greatly improved by the present stabilization method. As shown in Figure 12(b),

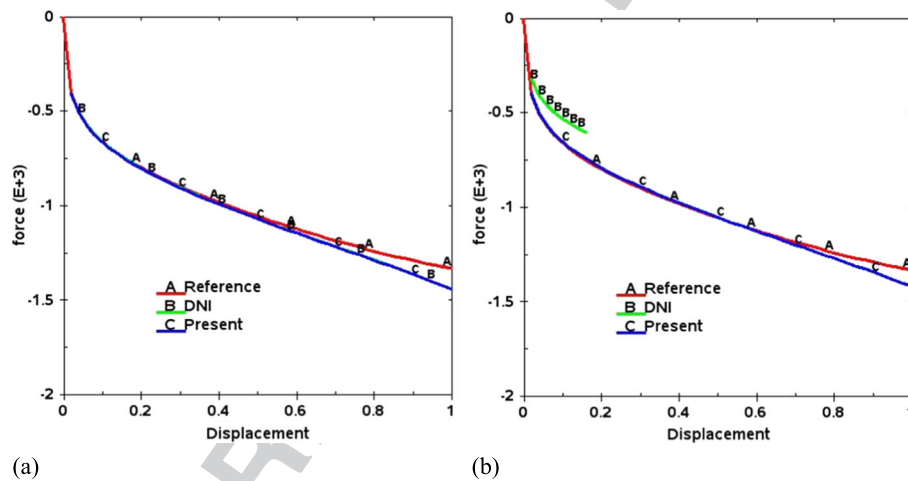


Figure 19. Comparison of reaction force response in quasi-static analysis. (a) uniform discretization and (b) nonuniform discretization.

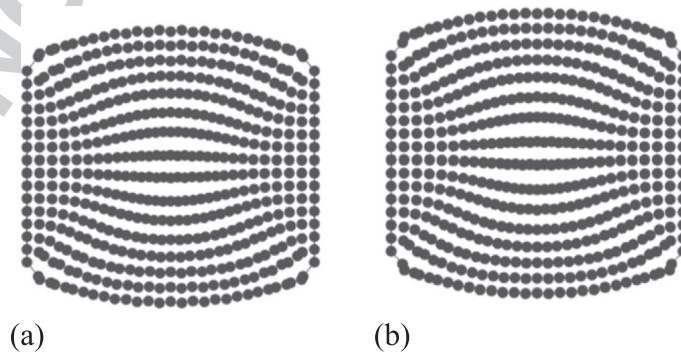


Figure 20. Comparison of deformation with uniform discretization in quasi-static analysis. (a) direct nodal integration ($d = 0.98$) and (b) present method ($d = 1.0$).

the present stabilization solution matches the reference solution very well in all three discretization models. No zero-energy modes are observed in the final deformation plots as shown in Figure 14, and the deformation results are comparable with those obtained from the quasi-static analysis.

In the case of nonuniform discretization using the explicit dynamics analysis, the accuracy of the DNI method decreases significantly. The force response in Figure 15(a) and the deformation plots in Figure 16 present the noticeable errors in the DNI solution compared with those in the uniform discretization model. On the other hand, the present stabilization method in the nonuniform discretization predicts the force response that is as accurate as that in the uniform discretization. The enhanced accuracy in the present method is also demonstrated in the stable deformation at the final stage as depicted in Figure 17. Similar to the effective plastic strain distribution in the quasi-static analysis, two results using the uniform and nonuniform discretization in the explicit dynamic analysis are comparable as shown in Figure 18(a) and (b), respectively. Those accurate results of the present method indicate the effectiveness of the proposed SGS in the inelastic analysis.

5.2. Compression test

The same discretization model containing 496 nodes in the previous tension test is utilized for the compression test. Both the uniform and nonuniform discretization models are considered in this test. The reference solution is obtained from the meshfree-enriched finite element method [27, 28] using the uniform discretization model and quasi-static analysis for comparison. A total of 50 loading steps are used for the quasi-static analysis.

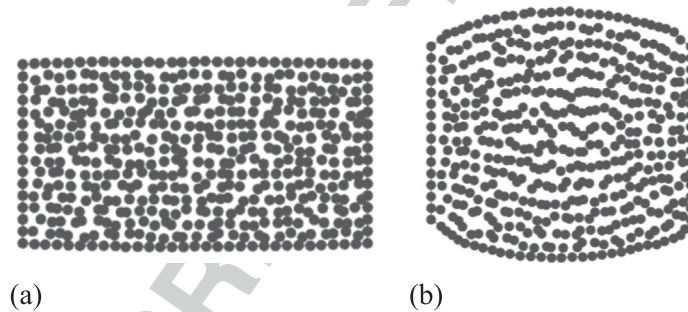


Figure 21. Comparison of deformation with nonuniform discretization in quasi-static analysis. (a) direct nodal integration method ($d = 0.16$) and (b) present method ($d = 1.0$).

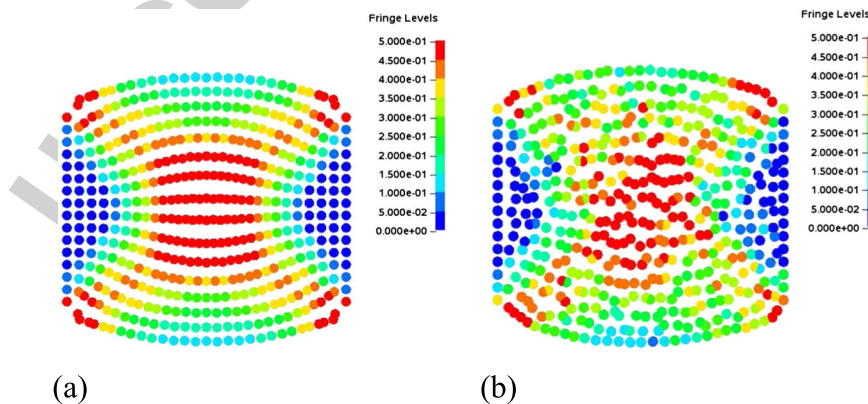


Figure 22. Comparison of effective plastic strain of present method at $d = 1.0$ in quasi-static analysis. (a) uniform discretization and (b) nonuniform discretization.

5.2.1. *Quasi-static analysis.* The comparison of reaction force response is given in Figure 19(a) and (b) for the uniform and nonuniform discretization, respectively. In the case of uniform discretization, the DNI solution agrees well with the present solution before the DNI method diverges at the compression displacement of 0.98. Compared with the uniform discretization solution, the nonuniform discretization solution of DNI method reacts overly soft and diverges much earlier as shown in Figure 19(b). This numerical behavior is very similar to the one in the tension test and is a cause of zero-energy modes in the DNI method. On the other hand, the present method consistently performs well in terms of force response in Figure 19 and the deformation in Figures 20 and 21 for uniform and nonuniform discretization, respectively. The present method also gives a comparable result in the effective plastic strain distribution as shown in Figure 22.

5.2.2. *Explicit dynamic analysis.* The reaction force results of uniform and nonuniform discretization are given in Figure 23(a) and (b), respectively. In the case of explicit dynamics analysis using the uniform discretization, the DNI method performs poorly in comparison with the results of quasi-static analysis. As shown in Figure 23(a), a major numerical breakdown in the DNI method is caused by the zero-energy modes as displayed in Figure 24(a) at the compression displacement of 0.8. The use of nonuniform discretization in the DNI method is clearly less accurate and produces more unstable deformation modes as shown in Figures 23(b) and 25(a) for the reaction force response and the final deformation, respectively. As opposed to the DNI method, the present method is able to deliver

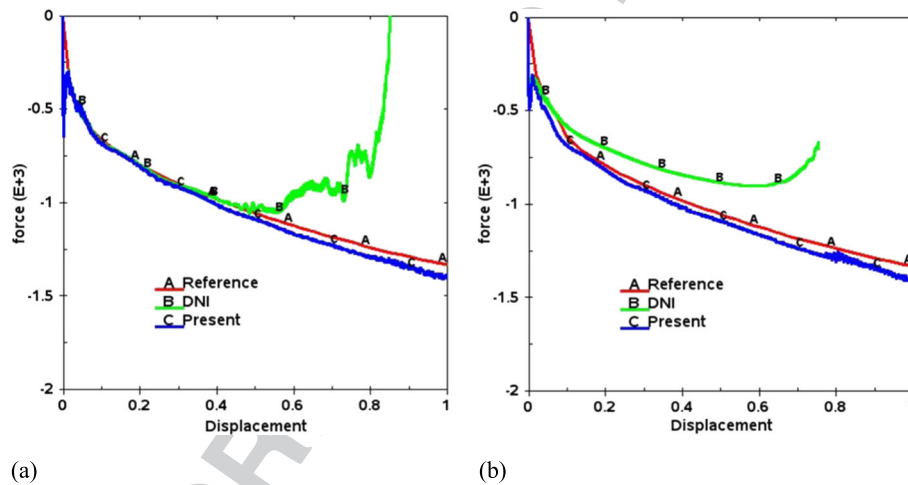


Figure 23. Comparison of reaction force response in quasi-static analysis. (a) uniform discretization and (b) nonuniform discretization.

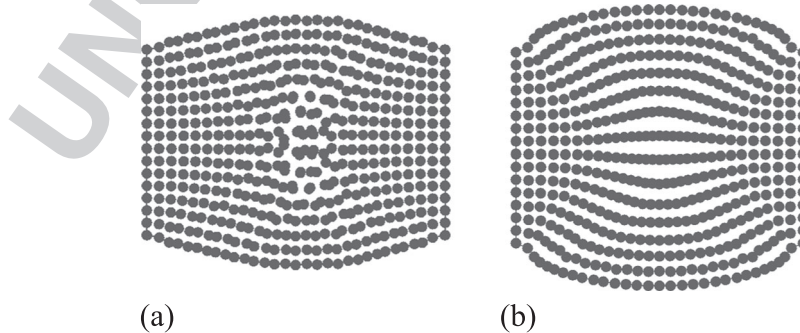


Figure 24. Comparison of deformation with uniform discretization in explicit dynamic analysis. (a) direct nodal integration (at $d = 0.8$) and (b) present method (at $d = 1.0$).

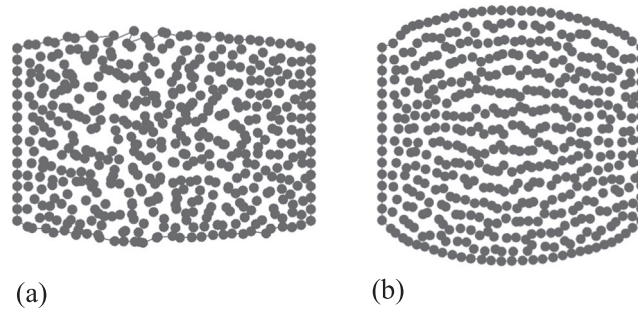


Figure 25. Comparison of deformation with nonuniform discretization in explicit dynamic analysis. (a) direct nodal integration integration (at $d = 0.7$) and (b) present method (at $d = 1.0$).

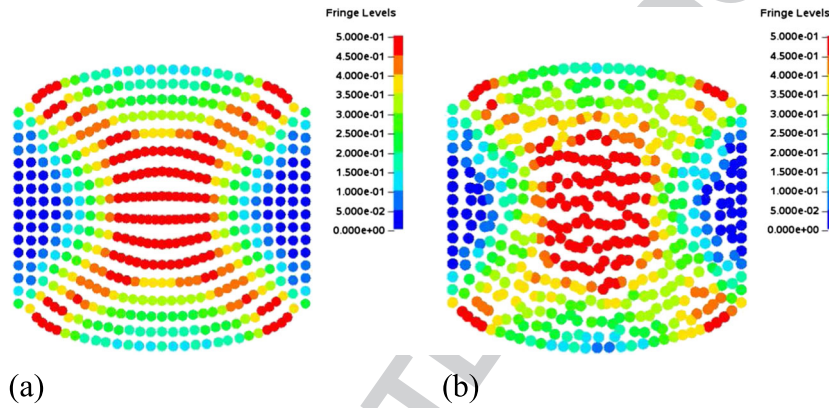


Figure 26. Comparison of effective plastic strain of present method at $d = 1.0$ in explicit dynamic analysis. (a) uniform discretization and (b) nonuniform discretization.

an accurate result using either the uniform or the nonuniform discretization as shown Figure 23. The final deformation plots displayed in Figures 24(b) and 25(b) show that the stable deformation modes are achieved using the proposed SGS. The comparable results of the uniform or nonuniform discretization in the effective plastic strain distribution as shown in Figure 26 indicate the applicability of the present method for the inelastic analysis in compression mode.

5.3. Severe deformation test

In this example, the compression in Example 5.2 is pushing much further for the severe deformation study. Because the meshfree-enriched finite element method [27, 28] diverges at the compression displacement of 1.02, the reference solution is not provided in this example. The DNI solution is also not included for comparison because of the divergence of solution in the early stage as reported in the previous example. Both quasi-static and explicit dynamics analyses with uniform discretization are considered for this study. The approach of adaptive anisotropic Lagrangian kernel described in Section 4 is employed in the proposed stabilization method to avoid the negative volume problem in this severe deformation analysis. The anisotropic Lagrangian kernel is updated at each implicit time step in the quasi-static analysis. A total of 100 constant time steps are utilized in the quasi-static analysis to reach the final compression displacement at 2.0. In the explicit dynamics analysis, the update of anisotropic Lagrangian kernel is carried out every 500 explicit time steps.

Figure 27 compares the reaction force response using the quasi-static and explicit dynamic analyses. As shown in Figure 27, both analyses predict similar force responses. Figure 28(a) and (b) presents the deformation history using the quasi-static and explicit dynamic analyses, respectively. The results indicate that the present method is capable of modeling the severe deformation problem

in this compression test. Figure 29 displays the effective plastic strain contour where the comparable high gradient patterns are obtained. Figure 30 reports the percentage of volume change in the compression test. Both analysis results generate a final volume change that is less than 1% in this inelastic analysis.

5.4. Necking of a 3D bar

To demonstrate the applicability of present formulation in the general 3D problem, the necking of a metal bar is tested. The 3D bar is 53.334 mm in length and 6.413 mm in radius. Similar to the simple

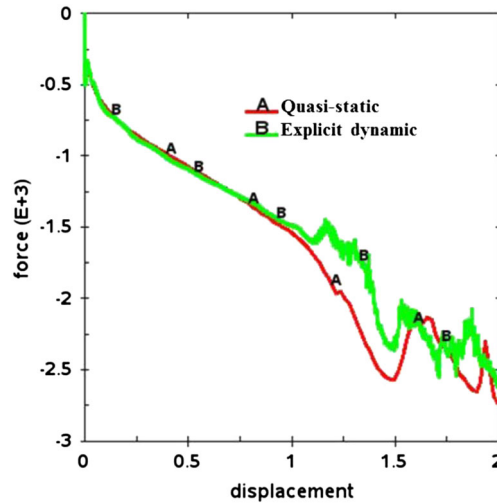


Figure 27. Comparison of force response in compression test.

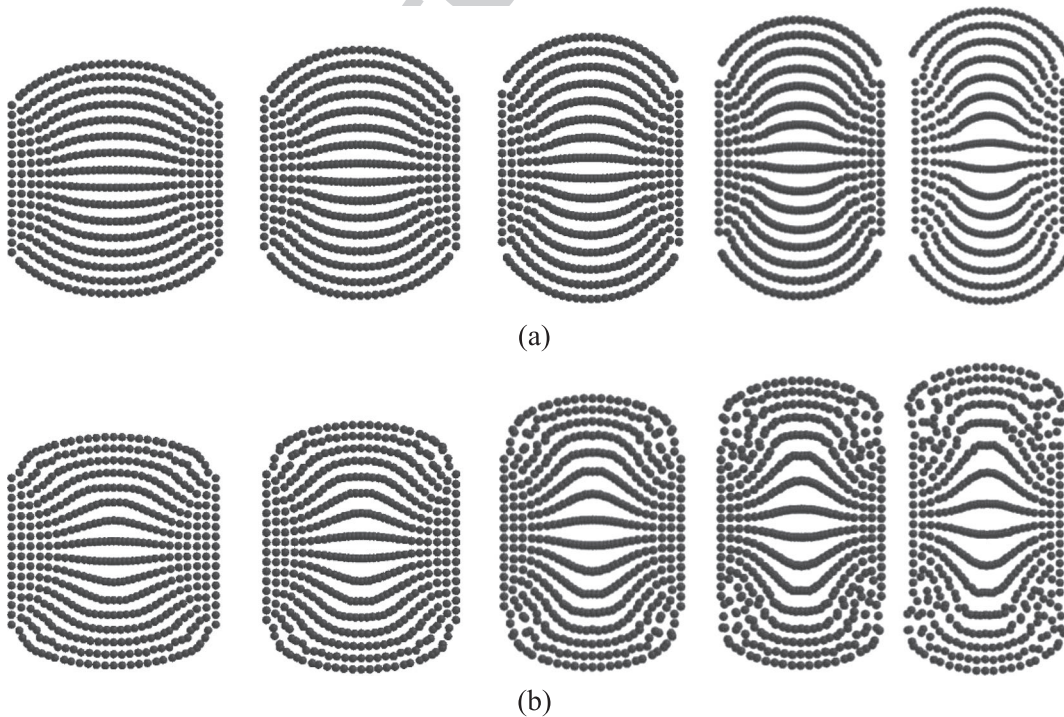


Figure 28. Deformation history in severe deformation test. (a) quasi-static analysis and (b) explicit dynamic analysis.

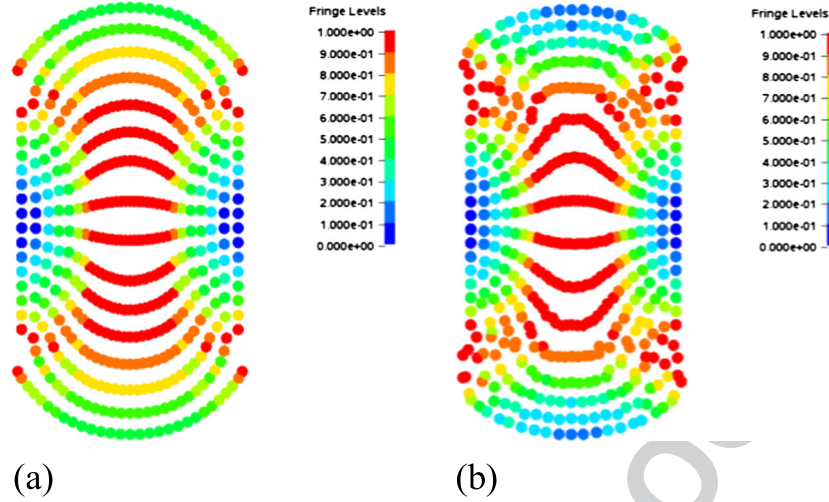


Figure 29. Comparison of effective plastic strain of present method at $d = 2.0$. (a) quasi-static analysis and (b) explicit dynamic analysis.

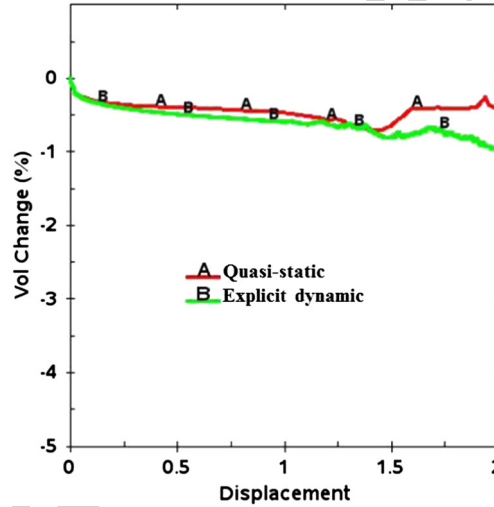


Figure 30. The percentage of volume change in compression test.

tension test in Example 5.1, one end of the specimen is fully constrained, and the other end is constrained and subjected to a displacement control to reflect the actual experimental test fixture [38]. In order to simulate necking, a geometric imperfection is introduced by a linear reduction in radius along the length, with radius at the center to be 98.2% of the radius at the end [26]. The material constants of the metal bar are as follows [1, 26]: Young's modulus $E = 206.9$ GPa, Poisson's ratio $\nu = 0.29$, density $\rho^0 = 7860$ kg/m³, and the isotropic hardening rule $\sigma_y(\bar{\epsilon}^p) = \sigma_y^0 + \alpha \bar{\epsilon}^p + (\sigma_y^\infty - \sigma_y^0)(1 - e^{-\beta \bar{\epsilon}^p})$ with coefficients $\beta = 16.93$, $\sigma_y^0 = 0.45$ GPa, $\sigma_y^\infty = 0.715$ GPa and $\alpha = 0.12924$ GPa. Both finite element method and present method are considered in the necking simulation using the explicit dynamics analysis, and the results are compared with experimental data [38]. The finite element analysis model is composed of 4200 hexahedra elements (4756 nodes) as shown in Figure 31. One-point integration with hourglass control is adapted for the finite element analysis [39]. The same discretization is used for the meshfree analysis based on the proposed formulation.

The deformed geometries are plotted in Figure 32 (a) and (b) for the finite element analysis and the present method, respectively. Figure 33(a) presents the load–displacement response. In Figure 33(a), the force result is normalized with the maximum load. Analogously, the displacement is normalized

F31

F32

F33

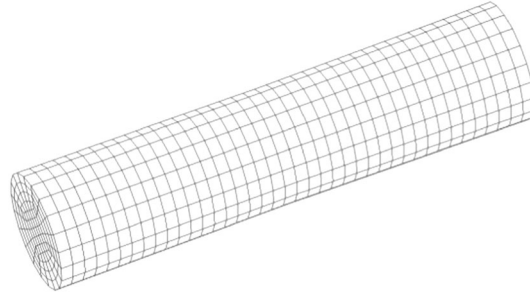


Figure 31. The finite element mesh of 3D bar in necking problem.

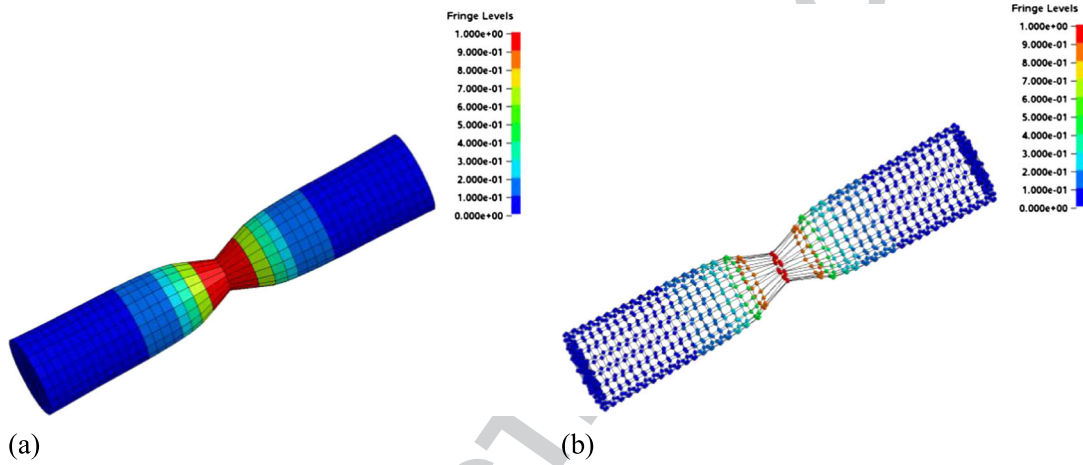


Figure 32. Deformed configuration of 3D bar in effective plastic strain contour. (a) finite element method and (b) present method.

with a length of gauge $L_0 = 50.8$ mm [26]. Both numerical results match very well before necking. Although visible difference is observed in the load–displacement curve when the bar starts to have necking, both finite element method and present method predict the results that are still compared favorably with the experimental data [38]. The response of normalized neck radius is also investigated. Good agreement between experimental data and the present meshfree solution is shown in Figure 33(b).

5.5. 3D metal grooving simulation

This problem is studied to identify the applicability of the proposed formulation in 3D severe deformation analysis. A metal block of size $0.1\text{ m} \times 0.06\text{ m} \times 0.02\text{ m}$ is fixed at the bottom and grooved by a rigid rotating roller as shown in Figure 34. The width of the roller is 0.008 m. The roller has a constant rotating speed $\omega = 125$ rad/s and is traveling at a transverse speed $V = 0.5$ m/s. For present purpose, we further assume that the grooving process is isothermal, and frictional coefficient for the contact between roller and work piece is 0.1 . The material has an initial density of $\rho^0 = 2700$ kg/m³. The strain-hardening elastic-plastic material properties are as follows: Young's modulus $E = 70.0$ GPa, Poisson's ratio $\nu = 0.3$, and an isotropic hardening rule $\sigma_y(\bar{\epsilon}^p) = \sigma_y^0 + \gamma E_p \bar{\epsilon}^p$ with coefficients $\gamma = 1.0$, $\sigma_y^0 = 0.1$ GPa, and $E_p = 1.5e - 2$ GPa. The finite element analysis model for the work piece contains 15,000 hexahedra elements (17,391 nodes) that are uniformly distributed as shown in Figure 34. For finite element methods [39], both one-point integration with hourglass control formulation (FEM1) and selective reduced integration formulation (FEM2) are considered for the comparison. Explicit dynamics analysis is conducted for this simulation.

F34

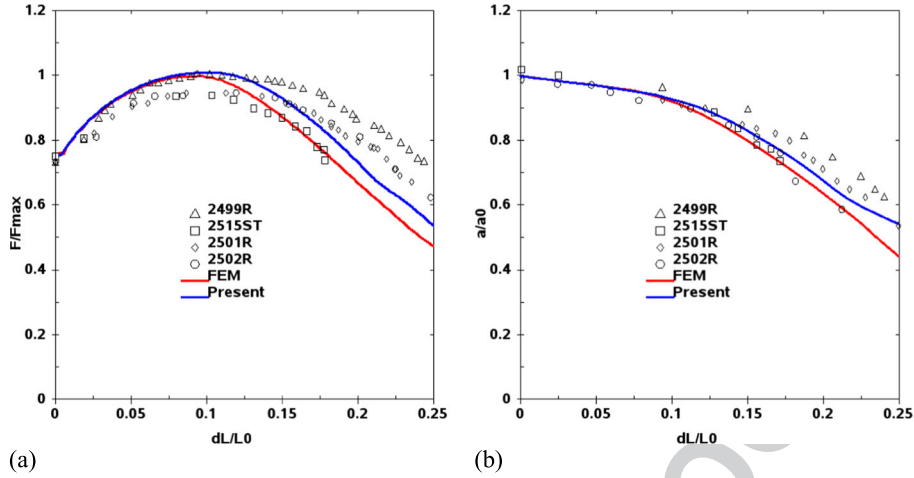


Figure 33. Comparison with experimental data. (a) normalized load F/F_{max} and (b) normalized neck radius a/a_0 .

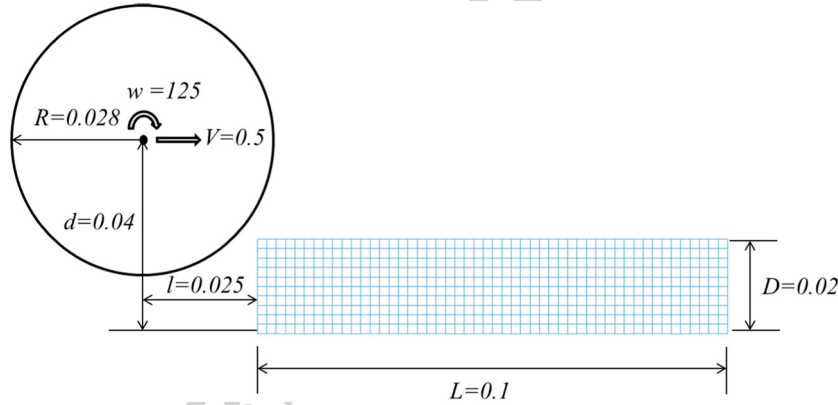


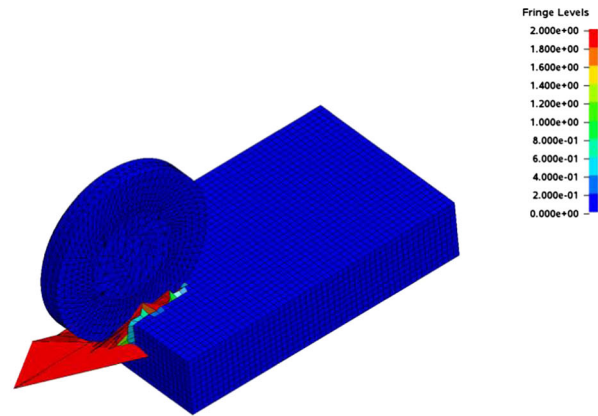
Figure 34. 3D metal grooving problem.

The final deformed geometries with effective plastic strain contours are plotted in Figure 35(a)–(c) for the FEM2, FEM1, and the present method, respectively. As shown in Figure 35(a), FEM2 method experiences severe mesh distortion problem, and the simulation stops in the early stage. Surprisingly, the FEM1 method improves the simulation in FEM2 and completes two-thirds of the simulation in grooving process as shown in Figure 35(b). On the other hand, the present method is able to accomplish the grooving simulation as depicted in Figure 35(c) for the final deformed geometry. It is worthwhile to note that the present method is very stable, and no shooting nodes are observed in the simulation. The comparisons of contact force in vertical and longitudinal directions are given in Figure 36(a) and (b), respectively. Good agreement between FEM1 solution and the present solution is shown in Figure 36 before FEM1 solution diverges. In contrast, the negative volume causes the FEM2 simulation to abort early as shown in the contact force response. Figure 37 presents the deformation history plotted in effective plastic contour using the present formulation.

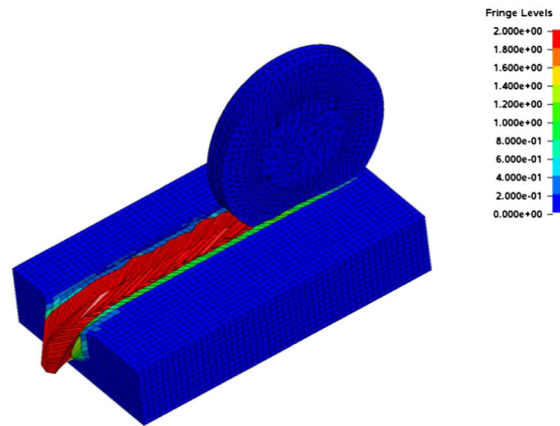
F35

F36

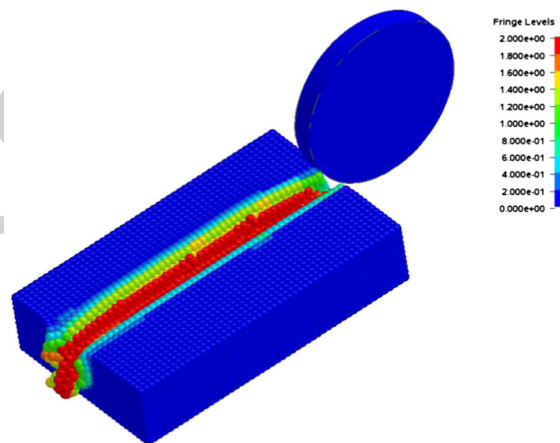
F37



(a)



(b)



(c)

Figure 35. Final deformation in the grooving problem. (a) FEM2; (b) FEM1; and (c) present method.

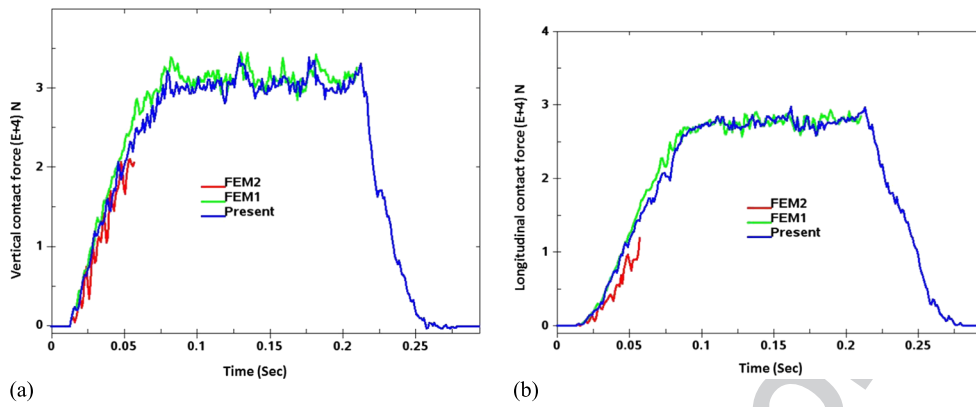


Figure 36. Comparison of contact force in the grooving problem. (a) vertical direction and (b) longitudinal direction.

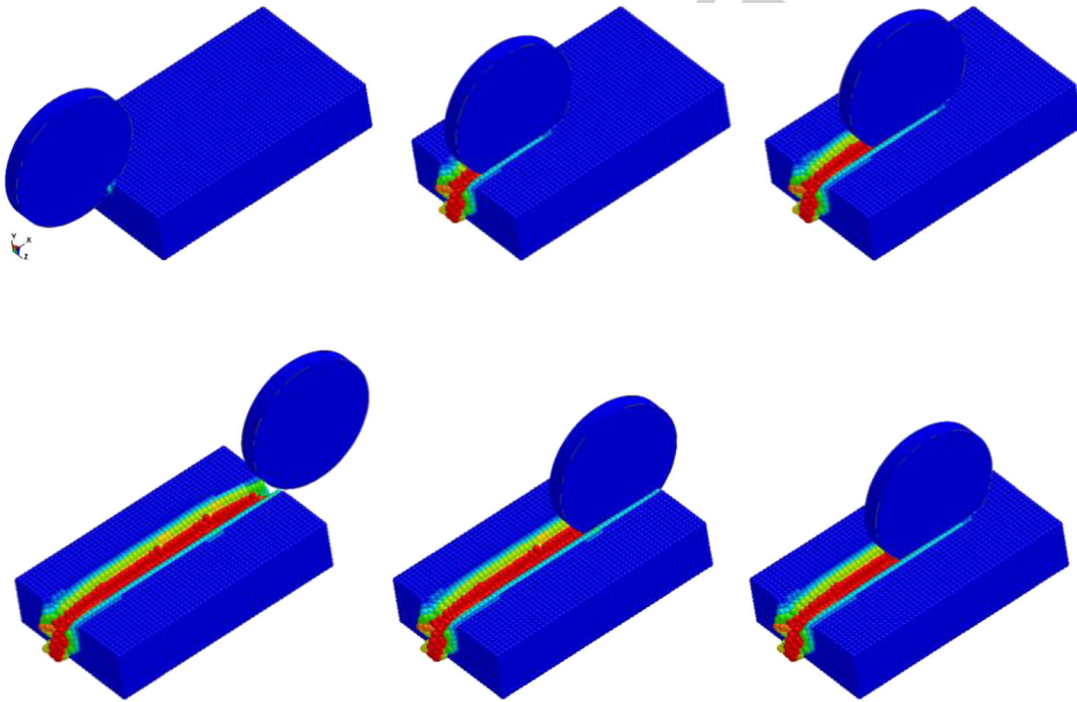


Figure 37. Deformation history in grooving simulation.

6. CONCLUSIONS

A purely nodal-integrated meshfree method is attractive from the viewpoint of formulation simplicity and simulation capability in the nonlinear analysis of solid mechanics problems. In this paper, the previous work of SGS method [22] for the linear elasticity analysis is generalized for the large deformation inelastic analysis. A nonlinear SGS formulation with dual nodal stress points is presented that is free from stabilization control parameters and integration cells for the meshfree computation. An adaptive anisotropic Lagrangian kernel approach is incorporated into the nonlinear SGS formulation to enhance the simulation capability for severe deformation analysis.

Our numerical results indicate that the present method is able to stabilize the meshfree DNI solution in the nonlinear analysis. It also has been demonstrated in the numerical examples that the

present nonlinear stabilized nodal integration method with the adaptive anisotropic Lagrangian kernel approach is capable of handling the severe deformation problem. One of the particular interests in the present method will be to analyze the damaged-induced strain localization problems. This demands a third-order displacement gradient for the regularization of nonlinear SGS formulation, which will be discussed in a separate paper.

ACKNOWLEDGEMENTS

The authors would like to thank Dr John O. Hallquist of LSTC for his support to this research. The support of this work by Yokohama Rubber Co., Ltd., Japan, under the Yosemite Project is gratefully acknowledged.

REFERENCES

1. Chen JS, Yoon S, Wu CT. Nonlinear version of stabilized conforming nodal integration for Galerkin meshfree methods. *International for Numerical Methods in Engineering* 2002; **53**:2587–2615.
2. Li S, Liu WK. *Meshfree Particle Method*. Springer: Berlin, 2004.
3. Puso MA, Chen JS, Zywicz W, Elmer W. Meshfree and finite element nodal integration methods. *International for Numerical Methods in Engineering* 2008; **74**:416–446.
4. Rabczuk T, Gracie R, Song HJ, Belytschko T. Immersed particle method for fluid–structure interaction. *International for Numerical Methods in Engineering* 2010; **81**:48–71.
5. Wu YC, Magallanes JM, Choi HJ, Crawford JE. An evolutionarily coupled finite element-meshfree formulation for modeling concrete behaviors under blast and impact loadings. *Journal of Engineering Mechanics* 2013; **139**:525–536.
6. Wu YC, Magallanes JM, Crawford JE. Fragmentation and debris evolution modeled by a point-wise coupled reproducing kernel/finite element formulation. *International Journal of Damage Mechanics* 2014; **23**:1005–1034.
7. Beissel S, Belytschko T. Nodal integration of the element-free Galerkin method. *Computer Methods in Applied Mechanics and Engineering* 1996; **139**:49–74.
8. Liu WK, Ong JSJ, Uras RA. Finite-element stabilization matrices – a unification approach. *Computer Methods in Applied Mechanics and Engineering* 1985; **53**:13–46.
9. Nagashima T. Node-by-node meshless approach and its applications to structural analyses. *International for Numerical Methods in Engineering* 1999; **46**:341–385.
10. Liu GR, Zhang GY, Wang YY, Zhong ZH, Li GY, Han X. A nodal integration technique for meshfree radial point interpolation method (NI-RPIM). *International Journal of Solids and Structures* 2007; **44**:3840–3860.
11. Chen JS, Wu CT, Yoon S, You Y. A stabilized conforming nodal integration for Galerkin meshfree methods. *International for Numerical Methods in Engineering* 2001; **50**:435–466.
12. Dyka CT, Randles PW, Ingel RP. Stress points for tension instability in SPH. *International for Numerical Methods in Engineering* 1997; **40**:2325–2341.
13. Chen JS, Wu YC, Guan PC, Theng H, Gaidos J, Hofstetter K, Alsaleh M. A semi-Lagrangian reproducing kernel formulation for modeling earth moving operations. *Mechanics of Materials* 2009; **41**:670–683.
14. Guan PC, Chi SW, Chen JS, Slawson RMJ. Semi-Lagrangian reproducing kernel particle method for fragment-impact problems. *International Journal of Impact Engineering* 2011; **38**:1033–1047.
15. Chi SW, Lee CH, Chen JS, Guan PC. A level set enhanced natural kernel contact algorithm for impact and penetration modeling. *International for Numerical Methods in Engineering* 2014; **102**:839–866.
16. Hillman M, Chen JS, Chi SW. Stabilized and variationally consistent nodal integration for meshfree modeling of impact problems. *Computational Particle Mechanics* 2014; **1**:245–256.
17. Chen JS, Hillman M, Rüter M. An arbitrary order variationally consistent integration method for Galerkin meshfree methods. *International for Numerical Methods in Engineering* 2013; **95**:387–418.
18. Wang D, Li Z. A two-level strain smoothing regularized meshfree approach with stabilized conforming nodal integration for elastic damage analysis. *International Journal of Damage Mechanics* 2013; **22**:440–459.
19. Wu YC, Wang DD, Wu CT. Three dimensional fragmentation simulation of concrete structures with a nodally regularized meshfree method. *Theoretical Applied Fracture Mechanics* 2014; **27**:89–99.
20. Chen JS, Wu CT, Belytschko T. Regularization of material instabilities by meshfree approximations with intrinsic length scales. *International for Numerical Methods in Engineering* 2000; **47**:1303–1322.
21. Wu CT, Guo Y, Hu W. An introduction to the LS-DYNA smoothed particle Galerkin method for severe deformation and failure analysis in solids. In *13th International LS-DYNA Users Conference*, Detroit, MI, June 8-10 2014; 1–20.
22. Wu YC, Wang D, Wu CT. A direct displacement smoothing meshfree particle formulation for impact failure modeling. *International Journal of Impact Engineering* 2015. DOI: 10.1016/j.ijimpeng.2015.03.013.
23. Wu CT, Koishi M, Hu W. A displacement smoothing induced strain gradient stabilization for the meshfree Galerkin nodal integration method. *Computational Mechanics* 2015; **56**:19–37.
24. Hughes TJR. *The Finite Element Method*. Dover Publications Inc.: New York, 2000.
25. Wu CT, Park CK, Chen JS. A generalized approximation for the meshfree analysis of solids. *International for Numerical Methods in Engineering* 2011; **85**:693–722.

26. Chen JS, Pan C, Wu CT, Liu WK. Reproducing kernel particle methods for large deformation analysis of non-linear structures. *Computer Methods in Applied Mechanics and Engineering* 1996; **139**:195–227.
27. Wu CT, Hu W, Chen JS. A meshfree-enriched finite element method for compressible and nearly incompressible elasticity. *International for Numerical Methods in Engineering* 2012; **90**:882–914.
28. Wu CT, Koishi M. Three-dimensional meshfree-enriched finite element formulation for micromechanical hyper-elastic modeling of particulate rubber composites. *International for Numerical Methods in Engineering* 2012; **91**:1137–1157.
29. Wu CT, Guo Y, Askari E. Numerical modeling of composite solids using an immersed meshfree Galerkin method. *Composites Part B* 2013; **45**:1397–1413.
30. Sukumar N. Construction of polygonal interpolants: a maximum entropy approach. *International for Numerical Methods in Engineering* 2004; **61**:2159–2181.
31. Cardoso RPR, Yoon JW, Cracio JJ, Barlat F, Cesar de Sa JMA. Development of a one point quadrature shell element for nonlinear applications with contact and anisotropy. *Computer Methods in Applied Mechanics and Engineering* 2002; **191**:5177–5206.
32. Rabczuk T, Belytschko T, Xiao SP. Stable particle methods based on Lagrangian kernels. *Computer Methods in Applied Mechanics and Engineering* 2004; **193**:1035–1063.
33. Belytschko T, Liu WK, Moran B. *Nonlinear Finite Elements for Continua and Structures*. Wiley: Chichester, 2000.
34. Belytschko T, Bindeman LP. Assumed strain stabilization of the eight node hexahedral element. *Computer Methods in Applied Mechanics and Engineering* 1993; **105**:225–260.
35. Belytschko T, Guo Y, Liu WK, Xiao SP. A unified stability analysis of meshless particle methods. *International for Numerical Methods in Engineering* 2000; **48**:1359–1400.
36. Park CK, Wu CT, Kan CD. On the analysis of dispersion property and stable time step in meshfree method using generalized meshfree approximation. *Finite Element in Analysis and Design* 2011; **47**:683–697.
37. Wu CT, Ren B. A stabilized non-ordinary state-based peridynamics for the nonlocal ductile material failure analysis in metal machining process. *Computer Methods in Applied Mechanics and Engineering* 2015; **291**:197–215.
38. Norris DM, Moran B, Scudder JK, Quinones DF. A computer simulation of the tension test. *Journal of the Mechanics and Physics of Solids* 1978; **26**:1–19.
39. *LS-DYNA Users' Manual*. Livermore Software Technology Corporation: Livermore, USA, 2015.

Author Query Form

Journal: International Journal for Numerical Methods in Engineering

Article: nme_5147

Dear Author,

During the copyediting of your paper, the following queries arose. Please respond to these by annotating your proof with the necessary changes/additions.

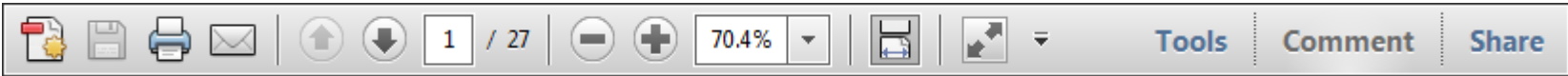
- If you intend to annotate your proof electronically, please refer to the E-annotation guidelines.
- If you intend to annotate your proof by means of hard-copy mark-up, please use the standard proofreading marks in annotating corrections. If manually writing corrections on your proof and returning it by fax, do not write too close to the edge of the paper. Please remember that illegible mark-ups may delay publication.

Whether you opt for hard-copy or electronic annotation of your proof, we recommend that you provide additional clarification of answers to queries by entering your answers on the query sheet, in addition to the text mark-up.

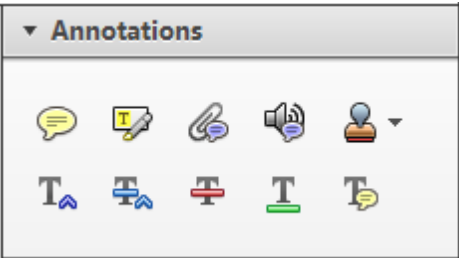
Query No.	Query	Remark
Q1	AUTHOR: Figures 4, 7, 8, 11, 12, 15, 18, 19, 22, 23, 26, 27, 29, 30, 32, 33, and 35–37 are recommended for color online and in print. Please check.	
Q2	AUTHOR: Please provide volume number and page range for Reference 22.	

Required software to e-Annotate PDFs: Adobe Acrobat Professional or Adobe Reader (version 7.0 or above). (Note that this document uses screenshots from Adobe Reader X)
The latest version of Acrobat Reader can be downloaded for free at: <http://get.adobe.com/uk/reader/>

Once you have Acrobat Reader open on your computer, click on the [Comment](#) tab at the right of the toolbar:



This will open up a panel down the right side of the document. The majority of tools you will use for annotating your proof will be in the [Annotations](#) section, pictured opposite. We've picked out some of these tools below:



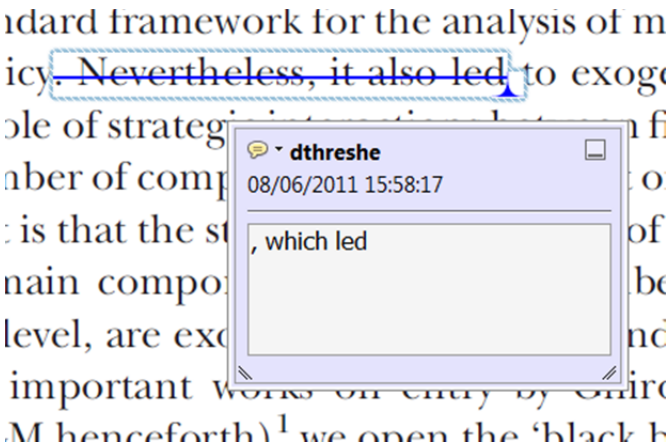
1. [Replace \(Ins\)](#) Tool – for replacing text.



Strikes a line through text and opens up a text box where replacement text can be entered.

How to use it

- Highlight a word or sentence.
- Click on the [Replace \(Ins\)](#) icon in the Annotations section.
- Type the replacement text into the blue box that appears.



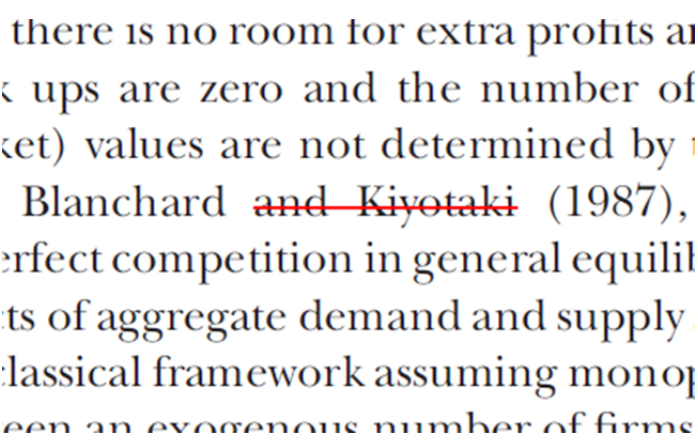
2. [Strikethrough \(Del\)](#) Tool – for deleting text.



Strikes a red line through text that is to be deleted.

How to use it

- Highlight a word or sentence.
- Click on the [Strikethrough \(Del\)](#) icon in the Annotations section.



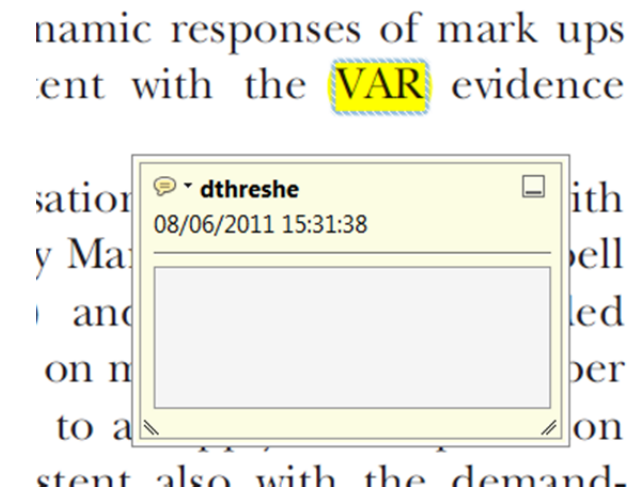
3. [Add note to text](#) Tool – for highlighting a section to be changed to bold or italic.



Highlights text in yellow and opens up a text box where comments can be entered.

How to use it

- Highlight the relevant section of text.
- Click on the [Add note to text](#) icon in the Annotations section.
- Type instruction on what should be changed regarding the text into the yellow box that appears.



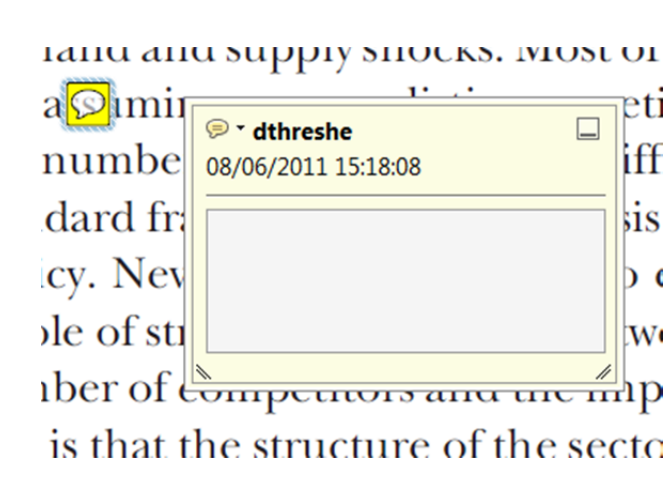
4. [Add sticky note](#) Tool – for making notes at specific points in the text.



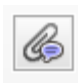
Marks a point in the proof where a comment needs to be highlighted.

How to use it

- Click on the [Add sticky note](#) icon in the Annotations section.
- Click at the point in the proof where the comment should be inserted.
- Type the comment into the yellow box that appears.

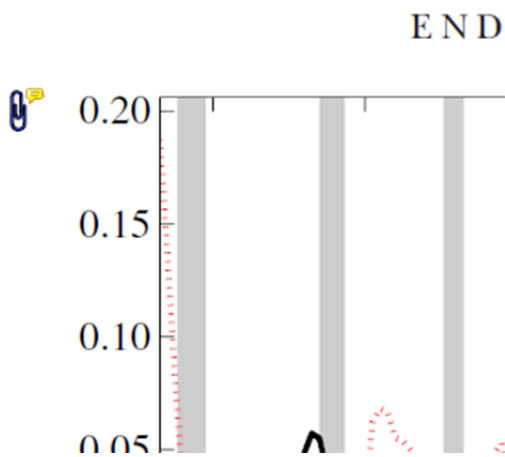


5. **Attach File** Tool – for inserting large amounts of text or replacement figures.


 Inserts an icon linking to the attached file in the appropriate place in the text.

How to use it

- Click on the **Attach File** icon in the Annotations section.
- Click on the proof to where you'd like the attached file to be linked.
- Select the file to be attached from your computer or network.
- Select the colour and type of icon that will appear in the proof. Click OK.



6. **Add stamp** Tool – for approving a proof if no corrections are required.

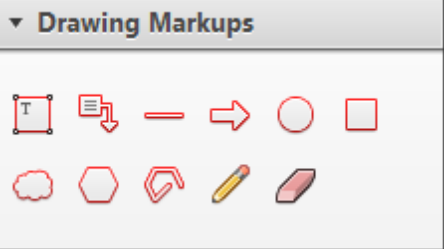
 Inserts a selected stamp onto an appropriate place in the proof.

How to use it

- Click on the **Add stamp** icon in the Annotations section.
- Select the stamp you want to use. (The **Approved** stamp is usually available directly in the menu that appears).
- Click on the proof where you'd like the stamp to appear. (Where a proof is to be approved as it is, this would normally be on the first page).

of the business cycle, starting with the
on perfect competition, constant return
production. In this environment goods
extra profits and the structure of market
he number of firms in the individual firm
etermined by the model. The New-Key
otaki (1987), has introduced product
general equilibrium models with nomin
ed and supply shocks. Most of this literat

APPROVED

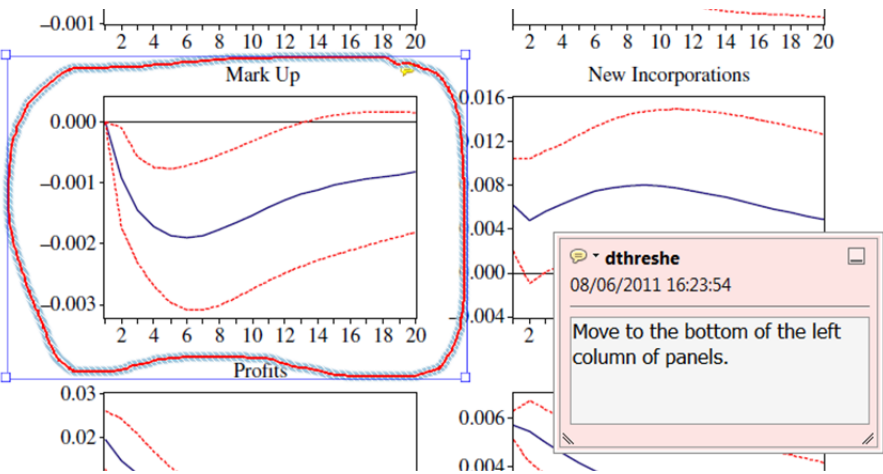


7. **Drawing Markups** Tools – for drawing shapes, lines and freeform annotations on proofs and commenting on these marks.

Allows shapes, lines and freeform annotations to be drawn on proofs and for comment to be made on these marks..

How to use it

- Click on one of the shapes in the **Drawing Markups** section.
- Click on the proof at the relevant point and draw the selected shape with the cursor.
- To add a comment to the drawn shape, move the cursor over the shape until an arrowhead appears.
- Double click on the shape and type any text in the red box that appears.



For further information on how to annotate proofs, click on the **Help** menu to reveal a list of further options:

